Article

GluA2-containing AMPA receptors form a continuum of Ca^{2+}-permeable channels

https://doi.org/10.1038/s41586-025-08736-2

Received: 25 March 2024

Accepted: 3 February 2025

Published online: 19 March 2025

Check for updates

Federico Miguez-Cabello[1,5], Xin-tong Wang[1,2,5], Yuhao Yan[1,2,5], Niklas Brake[3,4], Ryan P. D. Alexander[1,2], Amanda M. Perozzo[1,2], Anmar Khadra[3] & Derek Bowie[2]✉

Fast excitatory neurotransmission in the mammalian brain is mediated by cation-selective AMPA (α-amino-3-hydroxy-5-methyl-4-isoxazolepropionic acid) receptors (AMPARs)[1]. AMPARs are critical for the learning and memory mechanisms of Hebbian plasticity[2] and glutamatergic synapse homeostasis[3], with recent work establishing that AMPAR missense mutations can cause autism and intellectual disability[4–7]. AMPARs have been grouped into two functionally distinct tetrameric assemblies based on the inclusion or exclusion of the GluA2 subunit that determines Ca^{2+} permeability through RNA editing[8,9]. GluA2-containing AMPARs are the most abundant in the central nervous system and considered to be Ca^{2+} impermeable[10]. Here we show this is not the case. Contrary to conventional understanding, GluA2-containing AMPARs form a continuum of polyamine-insensitive ion channels with varying degrees of Ca^{2+} permeability. Their ability to transport Ca^{2+} is shaped by the subunit composition of AMPAR tetramers as well as the spatial orientation of transmembrane AMPAR regulatory proteins and cornichon auxiliary subunits. Ca^{2+} crosses the ion-conduction pathway by docking to an extracellular binding site that helps funnel divalent ions into the pore selectivity filter. The dynamic range in Ca^{2+} permeability, however, arises because auxiliary subunits primarily modify the selectivity filter. Taken together, our work proposes a broader role for AMPARs in Ca^{2+} signalling in the mammalian brain and offers mechanistic insight into the pathogenic nature of missense mutations.

α-Amino-3-hydroxy-5-methyl-4-isoxazolepropionic acid (AMPA)-type ionotropic glutamate receptors mediate most fast excitatory neurotransmission in the central nervous system[1]. They form the hardwiring of glutamatergic circuits but also strengthen or weaken synaptic transmission during periods of sustained patterned activity or altered homeostasis[11,12]. Different families of AMPA receptors (AMPARs)[13] shape the complex behaviour of neuronal circuits[14]. Early investigations concluded that the rapid and slow gating of native AMPARs expressed by interneurons and principal cells, respectively, reflected the differential expression of GluA2 and GluA4 AMPAR subunits[15,16], with the faster kinetics of GluA4 (ref. 17) being more dominant in interneurons[16]. This work led to the finding that interneurons and principal cells express AMPARs differing in their ability to transport Ca^{2+} (refs. 15,16). Interneurons with low levels of GluA2 were proposed to confer high Ca^{2+} permeability whereas higher GluA2 expression in principal cells accounted for the near lack of divalent permeability[15,16]. This distinction was further corroborated in recombinantly expressed receptors showing that RNA editing of the Q/R site selectivity filter of GluA2 rendered AMPARs Ca^{2+} impermeable and resistant to polyamine block whereas GluA2-lacking AMPARs composed of unedited GluA1, A3 and/or A4 subunits were Ca^{2+} permeable and sensitive to polyamine block[9,13,18–20]. These advances led to the understanding that the transport of Ca^{2+} by AMPARs is important in synapse strengthening[21–23] and can contribute to neurotoxicity with excessive activation[24–27].

Although insightful, this pioneering work preceded the discovery of distinct families of auxiliary subunits that co-assemble with AMPAR subunits. As such, AMPARs cannot be simply classified into GluA2-lacking and GluA2-containing AMPARs because this classification fails to account for the greater functional diversity found in native AMPAR–auxiliary protein complexes[1,28]. Recent work has established new fundamental rules for AMPAR assembly and functionality. First, almost all native AMPARs co-assemble with one of two claudin proteins called transmembrane AMPAR regulatory proteins (TARPs) or germ cell-specific gene 1-like protein (GSG1L). Co-assembly with TARPs falls into the type I class (that is, TARP γ2, γ3, γ4 and γ8) or the less abundant type II class (that is, TARP γ5 and γ7)[28,29], with GSG1L-containing AMPARs representing only 5% of all AMPARs[30]. Second, TARPs co-assemble with AMPARs either in a 4:4 or 2:4 stoichiometry[31–33], whereas GSG1L-containing AMPARs have a strict 2:4 stoichiometry[34,35]. Third, AMPAR-TARP complexes can co-assemble with other auxiliary proteins, most notably the cornichon (CNIH) family in an octameric arrangement[36,37]. Although SynDIG4/Prrt1 and the CKAMP family[28,29] have also been identified as auxiliary proteins, how they integrate into AMPAR complexes is still not fully understood[1,38–40]. Fourth and finally,

[1]Department of Pharmacology and Therapeutics, McGill University, Montreal, Quebec, Canada. [2]Integrated Program in Neuroscience, McGill University, Montreal, Quebec, Canada. [3]Department of Physiology, McGill University, Montreal, Quebec, Canada. [4]Quantitative Life Sciences PhD program, McGill University, Montreal, Quebec, Canada. [5]These authors contributed equally: Federico Miguez-Cabello, Xin-tong Wang, Yuhao Yan. ✉e-mail: derek.bowie@mcgill.ca

expression of AMPAR–auxiliary subunit complexes is apparently brain region specific with the cerebellum primarily expressing claudin-only AMPARs[30,31], whereas AMPARs containing the CNIHs, CKAMPs and SynDIG4/Prrt1 are found in the hippocampus and cortex[1,29,41,42].

Whether the co-assembly of GluA2-containing AMPARs with different families of auxiliary subunits affects their ability to transport Ca^{2+} has yet to be tested. A recent study has uncovered a new divalent binding pocket, called Site-G, that lies in the extracellular vestibule of the pore formed by the highly conserved SYTANLAAF amino acid motif that facilitates the transport of Ca^{2+} into the Q/R site selectivity filter[43]. The importance of Site-G is that it explains how GluA2-lacking AMPARs preferentially transport Ca^{2+}, even though Ca^{2+} is 70 times less abundant in the extracellular milieu than Na^+. The edited R-form of the GluA2 subunit possesses Site-G[43] raising the question whether co-expression with auxiliary subunits, particularly the TARPs and CNIHs, affects Ca^{2+} permeation of GluA2-containing AMPARs.

Ca^{2+}-permeable TARP-bound GluA2-AMPARs

To examine this, we compared the permeation properties of recombinant AMPARs of known subunit composition with native AMPARs expressed by cerebellar Purkinje cells and Bergmann glia that show low[44] and high[18] Ca^{2+} permeability, respectively, and thus act as a point of reference (Fig. 1). The permeability of Ca^{2+} relative to Na^+ (P_{Ca}/P_{Na}) was assessed by measuring the reversal potential (E_{rev}) of agonist-evoked membrane currents in solutions rich in either external Na^+ (150 mM NaCl) or Ca^{2+} (108 mM $CaCl_2$) (Fig. 1 and Methods). P_{Ca}/P_{Na} measured for AMPARs excised in outside-out patches from Purkinje cells and Bergmann glia was 0.08 ± 0.02 and 3.43 ± 0.56, respectively, consistent with GluA2-containing and GluA2-lacking receptors (Fig. 1a,b and Supplementary Table 1). In keeping with this, the relative divalent permeability of recombinant AMPARs assembled from GluA1/A2 subunits alone was 0.06 ± 0.01, which was similar (unpaired two-sided *t*-test, $P = 0.15$) to AMPARs expressed by Purkinje cells (Fig. 1a,c and Supplementary Table 1).

The impact of auxiliary subunit placement and stoichiometry on GluA2 AMPAR heteromers was studied by tethering two abundant TARP subunits, namely TARP-γ2 or TARP-γ8, to GluA1 or GluA2 alone or to both using a peptide linker (Methods). Previous work from our laboratory has shown that tethering TARP auxiliary subunits fully reproduces the gating properties of native AMPARs expressed in the mammalian brain[31,34] (Extended Data Fig. 1). As explained later, the tethering of TARPs to recombinant AMPARs also recapitulates the permeation properties of native channels.

Co-assembly of GluA1/A2 heteromers with either TARP-γ2 or TARP-γ8 induced a significant increase in Ca^{2+} permeability compared to GluA1/A2 alone (Fig. 1c–f, Extended Data Fig. 2a,b and Supplementary Table 1). The relative Ca^{2+} permeability was similar for TARP-γ2 when co-assembled at a subunit stoichiometry of 4:4 with either GluA1/A2 or GluA2/A3 heteromers (P_{Ca}/P_{Na} 0.14 ± 0.01 for GluA1-γ2/A2-γ2, 0.12 ± 0.01 for GluA2-γ2/A3-γ2) (Fig. 1c–f, Extended Data Fig. 2a,b and Supplementary Table 1). However, striking differences were observed with a stoichiometry of 2:4. Notably, Ca^{2+} permeability increased significantly when TARP-γ2 was tethered to the GluA2 subunit in GluA1/A2 heteromers (P_{Ca}/P_{Na} 0.43 ± 0.04, $n = 16$). This increase in Ca^{2+} permeability was not observed by tethering either TARP-γ2 or TARP-γ8 to GluA1 (P_{Ca}/P_{Na} 0.12 ± 0.01, $n = 5$ for GluA1-γ2/A2, 0.12 ± 0.01, $n = 5$ for GluA1-γ8/A2) or even TARP-γ8 to GluA2 (P_{Ca}/P_{Na} 0.18 ± 0.03, $n = 5$ for GluA1/A2-γ8) (Fig. 1c–f, Extended Data Fig. 2a,b and Supplementary Table 1). In all cases, we excluded possible contamination of our data with homomeric unedited GluA1(Q) AMPARs by ensuring that all *I–V* plots were linear and thus devoid of polyamine block (Extended Data Fig. 2c,d). In keeping with this, we performed *G–V* plot simulations to examine how varying the proportion of unedited Q-form AMPARs, which show strong voltage-dependent polyamine block, affect the *G–V* plots of GluA1/A2(R) heteromers (Extended Data Fig. 3). From these simulations, we concluded that homomeric GluA1(Q) AMPARs contribute no more than 1% to the data we have obtained (Extended Data Fig. 3b). Moreover, when we estimated the reversal potential needed to observe an increase in the relative Ca^{2+} permeability (P_{Ca}/P_{Na} of 0.95, described below for GluA1/A2(R) heteromers (Fig. 2), 75% of the entire response would have to be unedited AMPARs that would show strong voltage-dependent polyamine block (Extended Data Fig. 3b–d), which is not the case for our dataset. Therefore, taken together, our data establish that GluA2-containing AMPARs show different degrees of Ca^{2+} permeability, which is dependent on both the placement (GluA1 versus GluA2) and type (γ2 versus γ8) of the TARP auxiliary subunit.

Ca^{2+}-permeable CNIH-bound GluA2-AMPARs

As native AMPARs can also co-assemble with CNIH-2 or CNIH-3 auxiliary proteins[29], we tested whether CNIHs can further modulate divalent permeability of TARP-γ2-bound GluA1/A2 heteromers (Fig. 2). As before, we excluded the possible contamination by homomeric GluA1 AMPARs by ensuring that all *I–V* plots were linear (Extended Data Fig. 4a,b). The inclusion of CNIH-2 or -3 into TARP-γ2 AMPARs was confirmed by measuring several response characteristics (that is, deactivation, desensitization, off kinetics and steady-state and/or peak response) that together are uniquely modified by CNIHs (Fig. 2a,b, Extended Data Fig. 4c,d and Supplementary Tables 2, 6)[30]. Like other laboratories, we have overexpressed CNIHs in our experiments and assumed that AMPARs tethered to TARP γ2 fully assemble with CNIHs in an octameric arrangement[36,45]. We cannot, however, exclude the possibility of partial CNIH occupancy. Either way, our data shows that CNIHs have a profound effect on channel gating and Ca^{2+} permeability.

Contrary to our findings with TARPs, the optimal position for CNIH-2 or CNIH-3 was on the GluA1 subunit. P_{Ca}/P_{Na} values of CNIH-2 were 0.55 ± 0.11 and 0.15 ± 0.02 when co-expressed at the GluA1 and GluA2 positions respectively (Fig. 2a,c,d). CNIH-3 had an even greater impact on divalent permeability with estimated P_{Ca}/P_{Na} values of 0.95 ± 0.05 and 0.10 ± 0.01 when co-expressed in the GluA1 and GluA2 positions, respectively (Fig. 2b–d and Supplementary Table 1). Furthermore, mutation of Ala789 of GluA1 to a bulky Phe to attenuate CNIH modulation[46], eliminated the shift in divalent permeability (P_{Ca}/P_{Na} 0.16 ± 0.02, $n = 8$) (Extended Data Fig. 4f,g and Supplementary Table 1) demonstrating that CNIH-3 exerts its effect, at least in part, through the TM4 domain of the GluA1 subunit. Taken together, these data further extend our findings showing that the degree of divalent permeability of GluA2-containing AMPARs is shaped not only by the heteromer composition (GluA1/A2 versus A2/A3) but also by the auxiliary subunit type (TARP versus CNIH) and its placement (Figs. 1f, 2d, Extended Data Figs. 2b, 4g and Supplementary Table 1). In all cases, the assembled AMPARs were insensitive to cytoplasmic spermine block (Extended Data Figs. 2, 4) demonstrating that the pore architecture can be altered to accommodate the transport of Ca^{2+} without necessarily permitting access to bulkier polyamine molecules.

Ca^{2+} permeability of missense mutations

To explore the nature of Ca^{2+} permeability further, we studied three missense mutations in the pore region of the GluA2 subunit that have been linked to autism and intellectual disability[4] (Fig. 3a,b). From previous work, it has already been established that the Q/R and +4 sites are key determinants of AMPAR Ca^{2+} permeability[9,47]. Given the augmentation of Ca^{2+} permeability by auxiliary proteins we wanted to explore whether changing the pore composition itself is sufficient to replicate the effect. Specifically, we studied whether a missense mutation in either the selectivity filter Q/R site (R607E/G) or +4 site (D611N) altered the divalent ion permeation properties of GluA1/A2

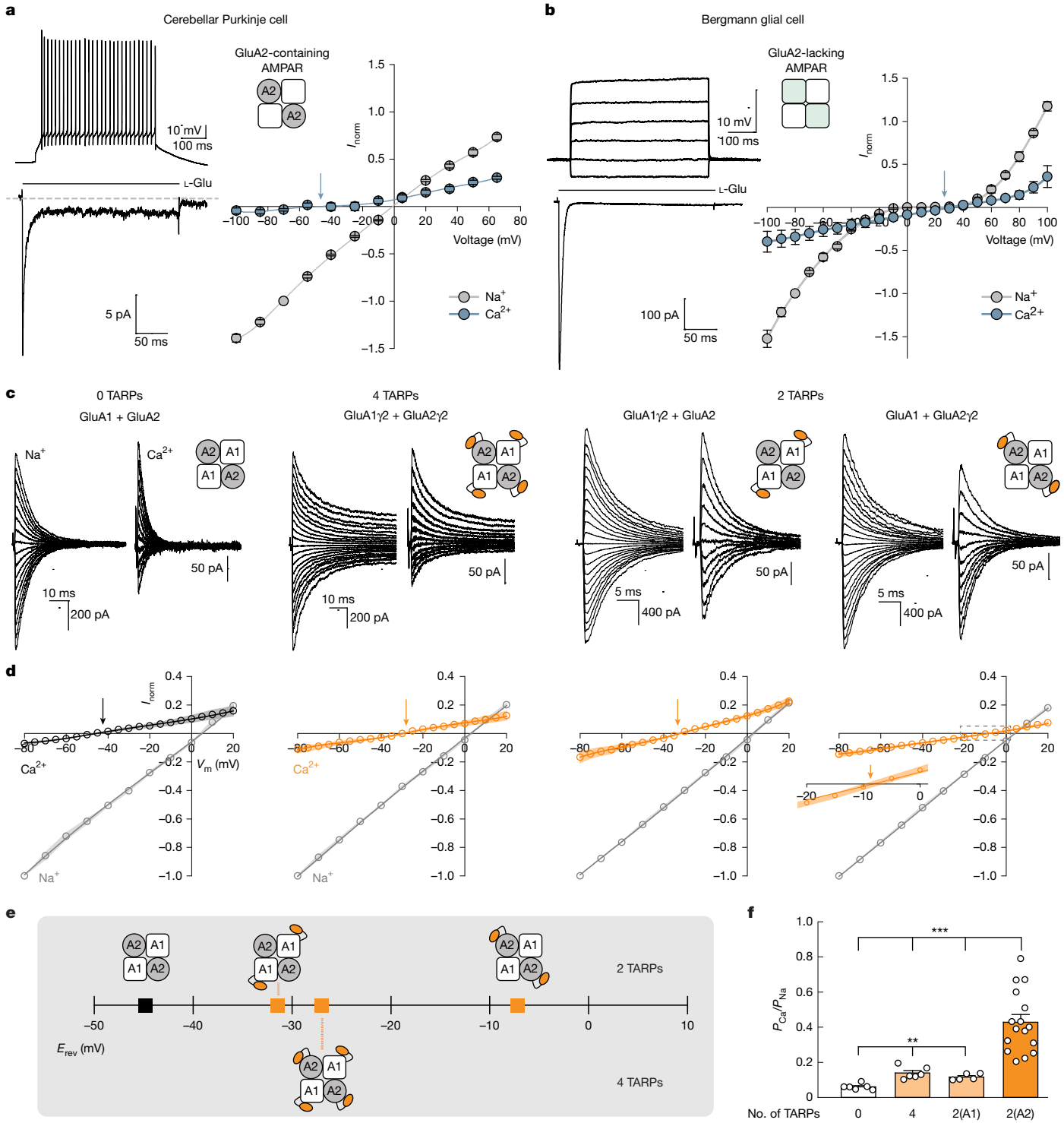

Fig. 1 | TARP γ2 regulates Ca^{2+} permeability of GluA2-containing AMPARs. **a**, Top left, typical action potential firing evoked by depolarizing current injection in a cerebellar Purkinje cell when depolarized in a current clamp recording (cell no. 190301C2, holding potential −70 mV, +200 pA step). Bottom left, voltage-clamp recording of an AMPAR response elicited by 10 mM L-Glu (250 ms) from an outside-out patch excised from a Purkinje cell (cell no. 190301C2, −60 mV). Right, current–voltage relationships of L-Glu patch responses of AMPARs expressed by Purkinje cells in Na^+ ($n = 8$) and Ca^{2+} ($n = 4$) rich external solutions. Note the negative reversal potential (arrow) in solutions rich in external Ca^{2+}. **b**, Top left, typical lack of action potential firing in a cerebellar Bergmann glial cell (cell no. 210210C3, holding potential −55 mV, −100 to +400 pA steps). Bottom left, voltage-clamp recording of an AMPAR response elicited by 10 mM L-Glu (250 ms) from an outside-out patch excised from a Bergmann glia (cell no. 210210C3, −60 mV). Right, current–voltage relationships of L-Glu patch responses of AMPARs expressed by Bergmann glial cells in Na^+ ($n = 7$) and Ca^{2+} ($n = 6$) rich external solutions. Note, the positive reversal potential (arrow) in solutions rich in external Ca^{2+}. **c**, Typical membrane currents elicited by 10 mM L-Glu at a range of membrane potentials for heteromeric GluA1/A2 receptors in the presence or absence of TARP γ2 (A1/A2 patch no. 190312p2; A1-γ2/A2-γ2 patch no. 190319p1; A1-γ2/A2 patch no. 190207p5; A1/A2-γ2 patch no. 190207p13). **d**, Current–voltage (normalized current, I_{norm}; voltage, V_m) plots of L-Glu responses in GluA1/A2 heteromers with/without TARP γ2 (A1/A2 $n = 6$; A1-γ2/A2-γ2 $n = 6$; A1-γ2/A2 $n = 5$; A1/A2-γ2: $n = 16$). **e**,**f**, Summary plots of reversal potentials of different GluA1/A2 heteromers (**e**) and their relative Ca^{2+} permeability (**f**) (two-sided Kruskal–Wallis analysis of variance (ANOVA) followed by Mann–Whitney *U*-tests with Bonferroni–Holm's correction, $^{**}P < 0.01$, $^{***}P < 0.001$). Data are mean ± s.e.m.

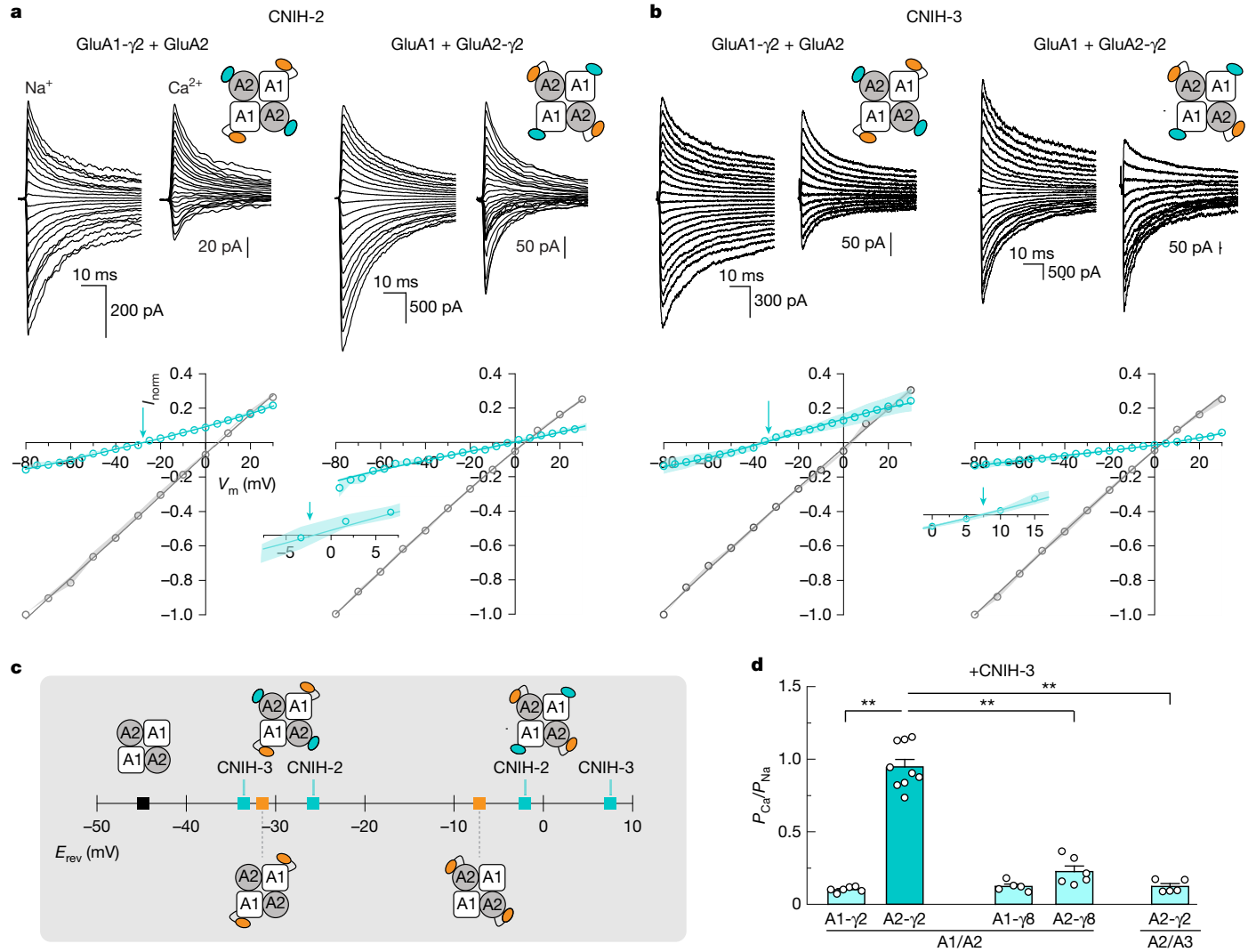

Fig. 2 | CNIHs further regulate Ca^{2+} permeability of GluA2-containing AMPARs. a,**b**, Top, typical membrane currents elicited by 10 mM L-Glu at a range of membrane potentials for TARP-γ2-bound GluA1/A2 receptors in the presence of CNIH-2 (**a**) (A1-γ2/A2 patch no. 210810p1; A1/A2-γ2 patch no. 210820p3) or CNIH-3 (**b**) (A1-γ2/A2 patch no. 190405p1; A1/A2-γ2 patch no. 190404p1). Bottom, current–voltage plots of L-Glu responses in TARP-γ2-bound GluA1/A2 heteromers with/without CNIHs (A1-γ2/A2 + CNIH-2 $n = 9$; A1 + CNIH-2/A2-γ2 $n = 8$; A1-γ2/A2 + CNIH-3 $n = 6$; A1 + CNIH-3/A2-γ2 $n = 9$). Cartoons depict GluA1/A2 octamers showing the position of the tethered TARP subunits and likely position of CNIHs. **c**,**d**, Summary plots of reversal potentials of TARP γ2 and CNIH-bound GluA1/A2 heteromers (**c**) and their relative Ca^{2+} permeability (**d**) (two-sided Kruskal–Wallis ANOVA followed by Mann–Whitney *U*-tests with Bonferroni–Holm's correction, $^{**}P < 0.01$). Data are mean ± s.e.m.

heteromers alone or when co-assembled with TARP-γ2 tethered to the GluA2 subunit (Fig. 3c,d).

Replacement of the positively charged Arg at the Q/R site with either Gly or Glu increased Ca^{2+} permeability of wild-type GluA1/A2 heteromers 25–50-fold from 0.06 ± 0.01 to 1.52 ± 0.11 ($n = 5$) or 3.51 ± 0.24 ($n = 5$), respectively (Fig. 3d, Extended Data Fig. 5a,b and Supplementary Table 1). The greater permeability observed by replacing Arg607 of GluA2 with Glu suggests that Ca^{2+} transport is optimized when the Q/R site has a net negative charge. Unlike wild-type receptors, both R607E and R607G mutant channels showed an appreciable block by cytoplasmic spermine (30 μM) with $K_{d(0mV)}$ values of 4.4 ± 0.9 μM ($n = 5$) and 34 ± 6.5 μM ($n = 4$), respectively (Fig. 3c and Extended Data Fig. 5c,d), suggesting that changes to the pore's architecture to augment Ca^{2+} transport also permit the larger polyamine cation molecule to enter and block. Tethering TARP-γ2 to GluA2 increased Ca^{2+} permeability further for the R607E (P_{Ca}/P_{Na} 4.65 ± 0.33, $n = 5$) and R607G (P_{Ca}/P_{Na} 2.35 ± 0.21, $n = 5$) (Fig. 3d, Extended Data Fig. 5e,f and Supplementary Table 1) mutants, demonstrating that missense mutations in the pore and TARP-γ2 have an additive effect. Co-assembly with TARP-γ2 had only a modest (R607E, $K_{d(0mV)}$ 14.5 ± 3.4 μM, $n = 7$) or no effect (R607G, $K_{d(0mV)}$ 38.2 ± 11.7 μM, $n = 5$) (Fig. 3c, Extended Data Fig. 5c–f and Supplementary Table 3) on attenuating polyamine block observed in wild-type AMPARs[10,48], suggesting that TARP-γ2 effects on Ca^{2+} permeability and polyamine block can be separable.

Unlike the Q/R site mutations, the missense mutation D611N at the +4 site did not cause a significant increase in Ca^{2+} permeability of GluA1/A2 heteromers alone (Fig. 3d and Extended Data Fig. 5). Although P_{Ca}/P_{Na} was increased almost threefold by tethering TARP-γ2 to GluA2 D611N (Fig. 3d and Supplementary Table 1), a similar change was observed in wild-type GluA1/A2 receptors (Fig. 3d and Supplementary Table 1). In all cases, the pore remained insensitive to block by cytoplasmic polyamine (Fig. 3c and Extended Data Fig. 5c–f). In conclusion, missense pore mutations at the Q/R site selectivity filter significantly augment Ca^{2+} permeability of GluA2-containing AMPARs, offering a likely explanation for their detrimental effects on the developing and adult brain in autism and intellectual disability. The missense mutation reported at the +4 site does not substantially alter pore divalent permeability (Extended Data Fig. 5), however, it hampers the surface expression of

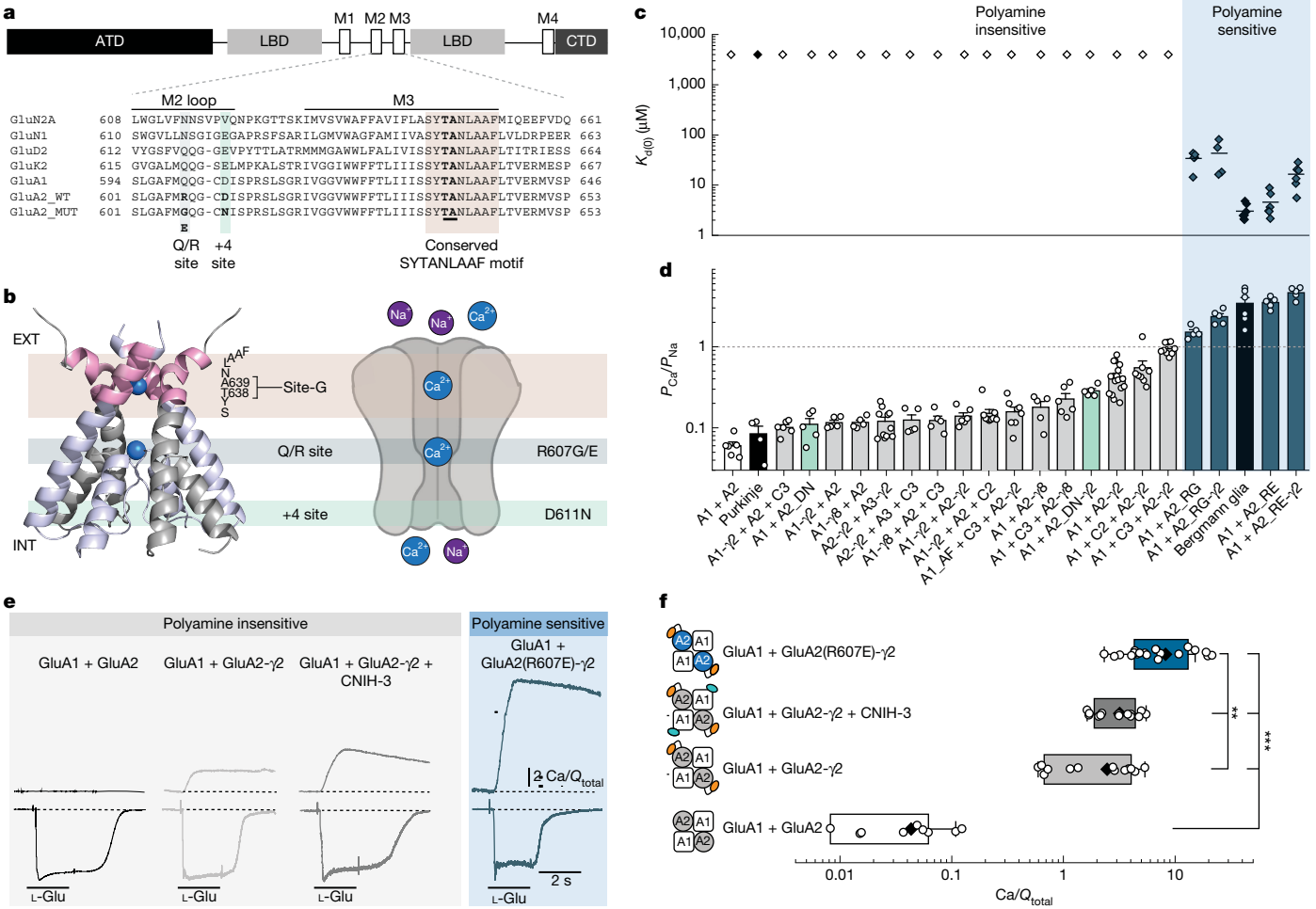

Fig. 3 | GluA2-containing AMPARs form a continuum of Ca^{2+} permeable channels. a, Sequence alignment of wild-type ionotropic glutamate receptor family members showing GluA2 missense mutations at the Q/R site and +4 site. **b**, AMPAR pore highlighting the location of the Q/R site and Site-G as Ca^{2+} binding sites with the +4 site in cryogenic-electron microscopy structure (left, PDB 7OCA) and cartoon form (right). **c**,**d**, Plots comparing the polyamine block sensitivity (K_d value measured at 0 mV, $K_{d(0mV)}$ using 30 μM spermine) (**c**) and the relative Ca^{2+} permeability (**d**) of different recombinant and native AMPARs. In the different combinations, A1 is GluA1, A2 is GluA2, A3 is GluA3, C2 and C3 are CNIH-2 and CNIH-3, respectively; mutations AF is A789F, DN is D611N, RG is R607G and RE is R607E. Dotted line denotes the point where Ca^{2+} permeable GluA2-containing AMPARs attain sensitivity to polyamine block. Data are mean ± s.e.m. **e**, Representative whole-cell membrane currents and concomitant cytoplasmic Ca^{2+} signal elicited by the activation of different AMPARs with 10 mM L-Glu (A1 + A2, cell no. 241110p3; A1/A2-γ2, cell no. 241114p9; A1 + CNIH-3/A2-γ2, cell no. 241115p4 and A1/A2(R607E)-γ2, cell no. 241101p2). **f**, Summary plot comparing the relative Ca^{2+} permeability of the different AMPARs tested (Ca/Q_{total} A1 + A2, 0.04 ± 0.01, n = 11; A1/A2-γ2, 2.46 ± 0.50, n = 13; A1 + CNIH-3/A2-γ2, 3.20 ± 0.33, n = 15 and A1/A2(R607E)-γ2, 8.18 ± 1.48, n = 18). Two-sided Kruskal–Wallis ANOVA followed by Mann–Whitney U-tests with Bonferroni–Holm's correction, $^{**}P < 0.01$, $^{***}P < 0.001$). Data are mean ± s.e.m. Credits: illustration in **b** adapted from ref. 36, Springer Nature Limited; diagram in **b** created using BioRender (https://biorender.com).

AMPAR heteromers[4] that will ultimately negatively affect the ability of AMPARs to transport Ca^{2+} at central synapses.

Differences in Ca^{2+} permeability among AMPARs was explored further by measuring L-Glu (10 mM) evoked whole-cell currents while simultaneously measuring the rise in cytoplasmic Ca^{2+} using the genetically encoded fast Ca^{2+} indicator, GCaMP6f (ref. 49) (Fig. 3e,f). Four AMPARs that together represent the entire range of divalent transport were chosen (Fig. 3d) and their ability to transport Ca^{2+} was represented as the ratio of the change in GCaMP6f fluorescence divided by the total charge transfer. As expected, GluA1/A2 heteromers failed to elicit a rise in cytosolic Ca^{2+} (Fig. 3e, left, 3f), in agreement with the poor divalent permeability estimated by the shift in reversal potential observed in Na^+ and Ca^{2+} rich external solutions (Fig. 1e,f). By contrast, activation of GluA1/A2(R607E) TARP-γ2 channels evoked a large and rapid rise in cytosolic Ca^{2+} (Fig. 3e, right, 3f), in good agreement with our estimates of P_{Ca}/P_{Na} (Fig. 3d). GluA1/A2 AMPARs assembled with TARP-γ2 alone or with CNIH-3 showed intermediate behaviour with measurable transport of external Ca^{2+} (Fig. 3e,f) but were insensitive to block by cytoplasmic spermine (30 μM) (Extended Data Fig. 6) further demonstrating that divalent permeability and polyamine block can be uncoupled.

Taken together with our earlier findings (Figs. 1, 2), these data show that GluA2-containing AMPAR heteromers form a continuum of Ca^{2+}-permeable ion channels (Fig. 3d) where the permeation pathway for Ca^{2+} is dynamically regulated by many factors including, (1) the type of AMPAR–auxiliary subunit (TARP versus CNIH) and (2) its placement within the tetramer, (3) the TARP isoform (TARP γ2 versus γ8) as well as (4) the specific amino acid that occupies the Q/R site. Contrary to current understanding, we show that GluA2-containing AMPARs can show appreciable Ca^{2+} permeability while remaining insensitive to block by polyamines (Fig. 3c,d). However, any change to the make-up of the AMPAR that renders Ca^{2+} permeability greater than Na^+ (Fig. 3d, dotted line), such as observed with missense mutations at the Q/R site, alters the pore's properties allowing polyamines to enter and cause channel block (Fig. 3c,d, blue shade). We therefore conclude that the pore of GluA2 AMPAR heteromers is designed to operate as a molecular sieve within a strict dynamic range where TARP and CNIH auxiliary subunits regulate

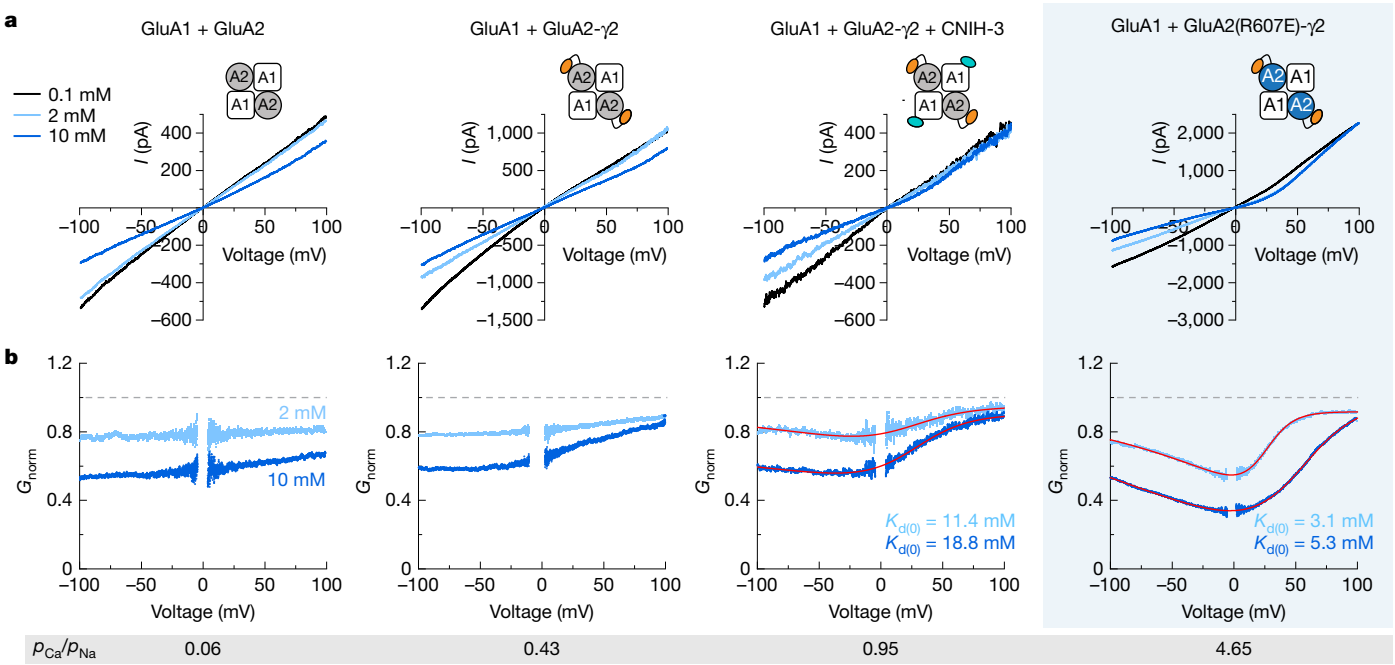

Fig. 4 | Block of GluA2-containing AMPARs by external Ca^{2+}. a, Current–voltage relationships of different AMPARs in different concentrations of external Ca^{2+} (0.1, 2 and 10 mM Ca^{2+}) (A1/A2 patch no. 230110p4; A1/A2-γ2 patch no. 230109p4; A1 + CNIH-3/A2-γ2 patch no. 230124p4; A1/A2-γ2 R607E patch no. 230302p1). **b**, Conductance–voltage plots showing the voltage dependency of block by 2 and 10 mM external Ca^{2+} (for 2 and 10 mM Ca^{2+}: A1/A2: $n = 4$ and 7; A1/A2-γ2: $n = 10$ and 12; A1 + CNIH-3/A2-γ2: $n = 7$ and 8; A1/A2-γ2 R607E: $n = 6$ and 8, respectively). Red line shows fit of the data to a single-binding site model of a permeant blocker (Methods). For more details see Supplementary Table 4.

channel opening permitting the passage of Ca^{2+} while preventing entry of polyamines by size exclusion. Whether auxiliary subunits achieve this by directly altering the pore diameter and/or modifying its electrostatic environment to affect ion transport, as noted previously[50], remains to be investigated. Either way, further expansion of the pore's architecture substantially augments Ca^{2+} transport with the trade-off that polyamine block occurs. As such, the need to avoid polyamine block sets a limit on the degree to which wild-type GluA2-containing AMPARs can show Ca^{2+} permeability. The fact that missense mutations of the Q/R site exceed this limit may be a defining characteristic that causally links them to the occurrence of autism and intellectual disability in patient groups.

AMPAR Ca^{2+} permeation from two sites

To determine where TARP and CNIH subunits act on the channel pore, we performed a more detailed comparison of the permeation properties of four AMPARs that differ in their ability to transport Ca^{2+} by almost two orders of magnitude (Fig. 4). Ca^{2+} traverses the pore of AMPARs by binding at two sites: Site-G that forms temporarily when the channel gate is activated[43] and the Q/R site selectivity filter[10]. Therefore, we reasoned that TARPs and/or CNIHs could augment Ca^{2+} permeability by acting exclusively on either Site-G or the Q/R site or a combination of both. We have shown previously that Ca^{2+} occupancy at each site can be interrogated by measuring the voltage dependence of block by external Ca^{2+} (ref. 43). Site-G lies outside the membrane electric field and therefore Ca^{2+} block is voltage-independent[43]. By contrast, the Q/R site lies within the membrane electric field making Ca^{2+} block voltage dependent[10,43,50]. Given this, block was measured at a range of membrane potentials to help pinpoint how auxiliary subunits enhance Ca^{2+} permeation through the pore (Fig. 4).

As expected, the voltage dependence of block varied substantially based on the relative Ca^{2+} permeability of each AMPAR. For example, Ca^{2+} block of GluA1/GluA2 receptors was only slightly voltage sensitive (Fig. 4b, left), presumably due to the positively charged Arg residue at the Q/R site of each GluA2 that oppose Ca^{2+} entry into the pore while also allowing access to Site-G. By contrast, co-assembly with TARP-γ2 alone or in combination with CNIH-3 rendered the block mechanism voltage dependent (Fig. 4b, centre left and right and Supplementary Table 4), which can be explained by Ca^{2+} accessing Site-G as well as the Q/R site within the membrane electric field. Finally, GluA1/A2 TARP-γ2 receptors containing the missense mutation, GluA2 R607E, showed striking voltage-dependent Ca^{2+} block (Fig. 4b, right), which is entirely in line with its marked divalent permeability (Fig. 3d and Supplementary Table 1). In support of this two-site ion-transport pathway, Ca^{2+} block was fit by the sum of two binding sites at all the membrane potentials tested. For example, at −100 mV, Ca^{2+} block was best fit by the sum of two binding sites of low and high affinity (Extended Data Fig. 7 and Supplementary Table 5), further demonstrating that block derives from a contribution of both Site-G and the Q/R site.

TARPs and CNIHs target the pore Q/R site

To further explore Ca^{2+} interactions between Site-G and the Q/R site, we compared the ability of different models of Ca^{2+} block to fit our data at all membrane potentials and external Ca^{2+} concentrations tested (Fig. 5 and Extended Data Fig. 8). We compared data fit to a single-binding site model (model 1) or double-binding site models (models 2–5) of Ca^{2+} block. For the double-binding site models, we assessed whether the data were better fit if Ca^{2+} block occurred in a sequential manner, such that occupancy of the first site, B1, preceded occupancy of the second site, B2 (models 2 and 3), or a non-sequential mechanism whereby Ca^{2+} block did not have this requirement (models 4 and 5). We also compared whether block occurred at both sites simultaneously (models 3 and 5) or only the single site B2 (models 2 and 4). The best model was chosen using the Bayesian information criterion (Extended Data Fig. 8c). In all cases, the voltage dependence of each binding site (B1 and B2) was not constrained but rather permitted to be determined by fits to the data.

Using this approach, Ca^{2+} block observed in all AMPARs was best explained by the non-sequential double-site model, model 4, whereby block depends on the occupancy of only one of the sites, B2 (Fig. 5a and

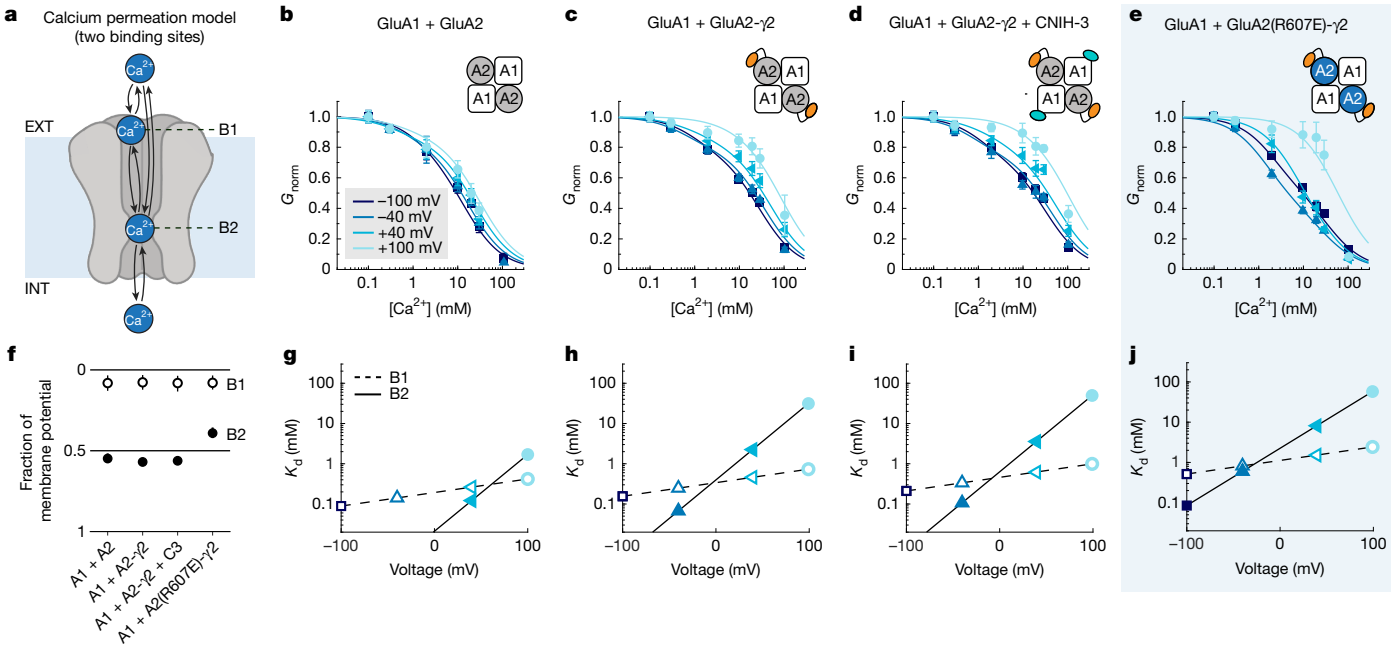

Fig. 5 | Permeation and block of GluA2-containing AMPARs by external Ca^{2+}. **a**, Cartoon showing the location of B1 and B2 sites of model 4 of the AMPAR. **b**–**e**, Ca^{2+} inhibition curves of four AMPARs at different membrane potentials and fit by model 4 (solid lines) determined to have the lowest Bayesian information criterion (**b** for GluA1 + GluA2, **c** for GluA1 + GluA2-γ2, **d** for GluA1 + GluA2-γ2 + CNIH-3 and **e** for GluA1 + GluA2(R607E)-γ2). **f**, Plot showing the similarity in the voltage dependency of B1 and B2 sites for all AMPARs tested. The exception is the B2 site, which is slightly less voltage dependent for AMPAR pore missense mutation, R607E. **g**–**j**, Ca^{2+} binding affinity for B1 and B2 sites at different membrane potentials for all AMPARs tested (**g** for GluA1 + GluA2, **h** for GluA1 + GluA2-γ2, **i** for GluA1 + GluA2-γ2 + CNIH-3 and **j** for GluA1 + GluA2(R607E)-γ2). Note the relative voltage-insensitivity of B1 and strong voltage sensitivity of B2. Diagram in **a** created using BioRender (https://biorender.com).

Extended Data Figs. 8–10). Parameter estimation of all AMPARs using model 4 revealed that Ca^{2+} occupancy of site B1 was mostly voltage insensitive, similar to Site-G[43], whereas occupancy and block at site B2 was strongly voltage sensitive, similar to the Q/R site[10,50], corresponding to roughly half of the total membrane potential, even in AMPARs with relatively voltage insensitive Ca^{2+} block (Fig. 5f). Moreover, the voltage dependency of B1 and B2 remained the same across all AMPAR heteromers, indicating that the binding sites remained in similar positions within the membrane electric field (Fig. 5f and Extended Data Fig. 10). This observation suggests that the variability in Ca^{2+} permeability among AMPARs is not due to differences in the location of binding sites within the pore. The exception to this was the GluA2 R607E AMPAR in which the voltage dependence of B2 differed slightly (Fig. 5f and Extended Data Figs. 9c,10b), consistent with missense mutations at the Q/R site altering the pore architecture to permit polyamine block. Ca^{2+} affinity of the two binding sites was strongly associated with Ca^{2+} permeability, with the affinity for site B2 becoming substantially lower with higher Ca^{2+} permeability (Fig. 5g–j and Extended Data Fig. 10c,d). On the basis of our experiments and modelling results, in conjunction with past studies[43], we conclude that TARP and CNIH auxiliary subunits control Ca^{2+} permeability of GluA2-containing AMPARs primarily by targeting the affinity of a voltage-sensitive Ca^{2+} binding site that most likely corresponds to the Q/R site.

Conclusion

For the last three decades, Ca^{2+} permeability of AMPARs was thought to be uniquely determined by the incorporation of the GluA2 subunit into tetrameric assemblies[1,51]. Our data establish that this is not the case. Instead, we show that GluA2-containing AMPARs form a continuum of Ca^{2+}-permeable ion channels, where divalent permeability is regulated within a strict dynamic range by TARPs and CNIHs by targeting the pore's selectivity filter. The fact that the same two-binding site model (Fig. 5) can fit Ca^{2+} block of AMPARs with an extensive range of divalent permeability (Fig. 4) further supports our assertion that they form a continuum. These observations agree well with the wide-ranging values of Ca^{2+} permeability reported for native AMPARs expressed by interneuron and principal cell populations across different brain regions[16]. Our findings also explain the apparent paradoxical observations showing that some native AMPARs can possess Ca^{2+} permeability in the absence of polyamine block, as noted for horizontal and AII amacrine cells of the retina[52], CA1 pyramidal cells of the hippocampus[53] and elsewhere (reviewed in ref. 13). The universal expression of the GluA2 subunit with TARP and CNIH proteins[28,29,54] suggests that the developing and adult mammalian brain possess many more divalent-permeable AMPARs than considered previously. It awaits future investigation whether widespread expression of divalent-permeable GluA2-containing AMPARs explains the occurrence of neurodevelopmental disorders when associated with missense mutations[4,7,55] or the excessive and neurotoxic transport of Ca^{2+} and/or Zn^{2+} linked to neurodegenerative disease as well as cerebral ischaemia[24,25,27].

Online content

Any methods, additional references, Nature Portfolio reporting summaries, source data, extended data, supplementary information, acknowledgements, peer review information; details of author contributions and competing interests; and statements of data and code availability are available at https://doi.org/10.1038/s41586-025-08736-2.

1. Hansen, K. B. et al. Structure, function, and pharmacology of glutamate receptor ion channels. *Pharmacol. Rev.* **73**, 298–487 (2021).
2. Nicoll, R. A. A brief history of long-term potentiation. *Neuron* **93**, 281–290 (2017).
3. Turrigiano, G. G. The self-tuning neuron: synaptic scaling of excitatory synapses. *Cell* **135**, 422–435 (2008).
4. Salpietro, V. et al. AMPA receptor GluA2 subunit defects are a cause of neurodevelopmental disorders. *Nat. Commun.* **10**, 3094 (2019).

5. Martin, S. et al. De novo variants in GRIA4 lead to intellectual disability with or without seizures and gait abnormalities. *Am. J. Hum. Genet.* **101**, 1013–1020 (2017).
6. Wu, Y. et al. Mutations in ionotropic AMPA receptor 3 alter channel properties and are associated with moderate cognitive impairment in humans. *Proc. Natl Acad. Sci. USA* **104**, 18163–18168 (2007).
7. Peall, K. J., Owen, M. J. & Hall, J. Rare genetic brain disorders with overlapping neurological and psychiatric phenotypes. *Nat. Rev. Neurol.* **20**, 7–21 (2024).
8. Sommer, B., Kohler, M., Sprengel, R. & Seeburg, P. H. RNA editing in brain controls a determinant of ion flow in glutamate-gated channels. *Cell* **67**, 11–19 (1991).
9. Burnashev, N., Monyer, H., Seeburg, P. H. & Sakmann, B. Divalent ion permeability of AMPA receptor channels is dominated by the edited form of a single subunit. *Neuron* **8**, 189–198 (1992).
10. Bowie, D. Polyamine-mediated channel block of ionotropic glutamate receptors and its regulation by auxiliary proteins. *J. Biol. Chem.* **293**, 18789–18802 (2018).
11. Herring, B. E. & Nicoll, R. A. Long-term potentiation: from CaMKII to AMPA receptor trafficking. *Annu. Rev. Physiol.* **78**, 351–365 (2016).
12. Turrigiano, G. G. The dialectic of Hebb and homeostasis. *Philos. Trans. R. Soc. Lond. B Biol. Sci.* **372**, 20160258 (2017).
13. Bowie, D. Redefining the classification of AMPA-selective ionotropic glutamate receptors. *J. Physiol.* **590**, 49–61 (2012).
14. Jonas, P. The time course of signaling at central glutamatergic synapses. *News Physiol. Sci.* **15**, 83–89 (2000).
15. Jonas, P., Racca, C., Sakmann, B., Seeburg, P. H. & Monyer, H. Differences in Ca2+ permeability of AMPA-type glutamate receptor channels in neocortical neurons caused by differential GluR-B subunit expression. *Neuron* **12**, 1281–1289 (1994).
16. Geiger, J. R. et al. Relative abundance of subunit mRNAs determines gating and Ca2+ permeability of AMPA receptors in principal neurons and interneurons in rat CNS. *Neuron* **15**, 193–204 (1995).
17. Mosbacher, J. et al. A molecular determinant for submillisecond desensitization in glutamate receptors. *Science* **266**, 1059–1062 (1994).
18. Burnashev, N. et al. Calcium-permeable AMPA-kainate receptors in fusiform cerebellar glial cells. *Science* **256**, 1566–1570 (1992).
19. Blaschke, M. et al. A single amino acid determines the subunit-specific spider toxin block of alpha-amino-3-hydroxy-5-methylisoxazole-4-propionate/kainate receptor channels. *Proc. Natl Acad. Sci. USA* **90**, 6528–6532 (1993).
20. Herlitze, S. et al. Argiotoxin detects molecular differences in AMPA receptor channels. *Neuron* **10**, 1131–1140 (1993).
21. Mahanty, N. K. & Sah, P. Calcium-permeable AMPA receptors mediate long-term potentiation in interneurons in the amygdala. *Nature* **394**, 683–687 (1998).
22. Liu, S. Q. & Cull-Candy, S. G. Synaptic activity at calcium-permeable AMPA receptors induces a switch in receptor subtype. *Nature* **405**, 454–458 (2000).
23. Plant, K. et al. Transient incorporation of native GluR2-lacking AMPA receptors during hippocampal long-term potentiation. *Nat. Neurosci.* **9**, 602–604 (2006).
24. Granzotto, A., Weiss, J. H. & Sensi, S. L. Editorial: excitotoxicity turns 50. The death that never dies. *Front Neurosci* **15**, 831809 (2021).
25. Kwak, S. & Weiss, J. H. Calcium-permeable AMPA channels in neurodegenerative disease and ischemia. *Curr. Opin. Neurobiol.* **16**, 281–287 (2006).
26. Weiss, J. H. & Sensi, S. L. Ca^{2+}-Zn^{2+} permeable AMPA or kainate receptors: possible key factors in selective neurodegeneration. *Trends Neurosci.* **23**, 365–371 (2000).
27. Cueva Vargas, J. L. et al. Soluble tumor necrosis factor alpha promotes retinal ganglion cell death in glaucoma via calcium-permeable AMPA receptor activation. *J. Neurosci.* **35**, 12088–12102 (2015).
28. Schwenk, J. et al. High-resolution proteomics unravel architecture and molecular diversity of native AMPA receptor complexes. *Neuron* **74**, 621–633 (2012).
29. Schwenk, J. et al. Functional proteomics identify cornichon proteins as auxiliary subunits of AMPA receptors. *Science* **323**, 1313–1319 (2009).
30. Perozzo, A. M., Brown, P. & Bowie, D. Alternative splicing of the flip/flop cassette and TARP auxiliary subunits engage in a privileged relationship that fine-tunes AMPA receptor gating. *J. Neurosci.* **43**, 2837–2849 (2023).
31. Dawe, G. B. et al. Nanoscale mobility of the apo state and TARP stoichiometry dictate the gating behavior of alternatively spliced AMPA receptors. *Neuron* **102**, 976–992 e975 (2019).
32. Zhao, Y., Chen, S., Swensen, A. C., Qian, W. J. & Gouaux, E. Architecture and subunit arrangement of native AMPA receptors elucidated by cryo-EM. *Science* **364**, 355–362 (2019).
33. Twomey, E. C., Yelshanskaya, M. V., Grassucci, R. A., Frank, J. & Sobolevsky, A. I. Elucidation of AMPA receptor-stargazin complexes by cryo-electron microscopy. *Science* **353**, 83–86 (2016).
34. Perozzo, A. M. et al. GSG1L-containing AMPA receptor complexes are defined by their spatiotemporal expression, native interactome and allosteric sites. *Nat. Commun.* **14**, 6799 (2023).
35. Twomey, E. C., Yelshanskaya, M. V., Grassucci, R. A., Frank, J. & Sobolevsky, A. I. Structural bases of desensitization in AMPA receptor-auxiliary subunit complexes. *Neuron* **94**, 569–580 e565 (2017).
36. Zhang, D., Watson, J. F., Matthews, P. M., Cais, O. & Greger, I. H. Gating and modulation of a hetero-octameric AMPA glutamate receptor. *Nature* **594**, 454–458 (2021).
37. Nakagawa, T. Structures of the AMPA receptor in complex with its auxiliary subunit cornichon. *Science* **366**, 1259–1263 (2019).
38. Matt, L. et al. SynDIG4/Prrt1 is required for excitatory synapse development and plasticity underlying cognitive function. *Cell Rep.* **22**, 2246–2253 (2018).
39. Diaz, E. Beyond the AMPA receptor: diverse roles of SynDIG/PRRT brain-specific transmembrane proteins at excitatory synapses. *Curr. Opin. Pharmacol.* **58**, 76–82 (2021).
40. Yu, J. et al. Hippocampal AMPA receptor assemblies and mechanism of allosteric inhibition. *Nature* **594**, 448–453 (2021).
41. Boudkkazi, S., Brechet, A., Schwenk, J. & Fakler, B. Cornichon2 dictates the time course of excitatory transmission at individual hippocampal synapses. *Neuron* **82**, 848–858 (2014).
42. von Engelhardt, J. et al. CKAMP44: a brain-specific protein attenuating short-term synaptic plasticity in the dentate gyrus. *Science* **327**, 1518–1522 (2010).
43. Nakagawa, T., Wang, X. T., Miguez-Cabello, F. J. & Bowie, D. The open gate of the AMPA receptor forms a $Ca^{(2+)}$ binding site critical in regulating ion transport. *Nat. Struct. Mol. Biol.* **31**, 688–700 (2024).
44. Tempia, F. et al. Fractional calcium current through neuronal AMPA-receptor channels with a low calcium permeability. *J. Neurosci.* **16**, 456–466 (1996).
45. Gangwar, S. P. et al. Modulation of GluA2-gamma5 synaptic complex desensitization, polyamine block and antiepileptic perampanel inhibition by auxiliary subunit cornichon-2. *Nat. Struct. Mol. Biol.* **30**, 1481–1494 (2023).
46. Hawken, N. M., Zaika, E. I. & Nakagawa, T. Engineering defined membrane-embedded elements of AMPA receptor induces opposing gating modulation by cornichon 3 and stargazin. *J. Physiol.* **595**, 6517–6539 (2017).
47. Dingledine, R., Hume, R. I. & Heinemann, S. F. Structural determinants of barium permeation and rectification in non-NMDA glutamate receptor channels. *J. Neurosci.* **12**, 4080–4087 (1992).
48. Brown, P., McGuire, H. & Bowie, D. Stargazin and cornichon-3 relieve polyamine block of AMPA receptors by enhancing blocker permeation. *J. Gen. Physiol.* **150**, 67–82 (2018).
49. Ohkura, M. et al. Genetically encoded green fluorescent Ca^{2+} indicators with improved detectability for neuronal Ca^{2+} signals. *PLoS ONE* **7**, e51286 (2012).
50. Bowie, D., Lange, G. D. & Mayer, M. L. Activity-dependent modulation of glutamate receptors by polyamines. *J. Neurosci.* **18**, 8175–8185 (1998).
51. Isaac, J. T., Ashby, M. C. & McBain, C. J. The role of the GluR2 subunit in AMPA receptor function and synaptic plasticity. *Neuron* **54**, 859–871 (2007).
52. Osswald, I. K., Galan, A. & Bowie, D. Light triggers expression of philanthotoxin-insensitive Ca^{2+}-permeable AMPA receptors in the developing rat retina. *J. Physiol.* **582**, 95–111 (2007).
53. Mattison, H. A. et al. Evidence of calcium-permeable AMPA receptors in dendritic spines of CA1 pyramidal neurons. *J. Neurophysiol.* **112**, 263–275 (2014).
54. Schwenk, J. et al. Regional diversity and developmental dynamics of the AMPA-receptor proteome in the mammalian brain. *Neuron* **84**, 41–54 (2014).
55. XiangWei, W. et al. Clinical and functional consequences of GRIA variants in patients with neurological diseases. *Cell. Mol. Life Sci.* **80**, 345 (2023).

Methods

Cell culture and transfection of HEK293T/17 cells

Human embryonic kidney 293T/17 (HEK293T/17) (ATCC) cells were maintained in MEM containing GlutaMAX. The media was supplemented with 10% fetal bovine serum (Gibco). Cells were plated at low density (1.6×10^4 cells per ml) on poly-D-lysine-coated 35-mm plastic dishes and were transiently transfected 48 h later using the calcium phosphate technique, as previously described[56]. After transfection, NBQX at a 30 μM final concentration was added to the media to avoid cell death. All experiments were performed using complementary DNA from previous publications from our group[31,48]. Single point mutations were performed on the plasmid vector mentioned previously. GluA and auxiliary subunits were cotransfected with plasmid vectors encoding eGFP to identify transfected cells as described elsewhere[30]. For tandem constructs GluA subunits and TARPs proteins were linked using seven amino acid linker (ELGTRGS).

In vitro patch-clamp electrophysiology recordings of recombinant AMPARs

Experiments were performed after 24 h of transfection. Agonist or antagonist solutions were applied to excised outside-out patches obtained from the transfected cells using a piezoelectric stack (Physik Instrumente). The solution exchange rate routinely had a 10–90% rise time of 25–50 μs, which was determined by measuring the liquid junction current at the end of each experiment[57]. To minimize electrical noise during recordings, a thick-walled, borosilicate glass pipette (3–6 MΩ) was coated with dental wax in conjunction with an Axopatch 200B amplifier (Molecular Devices). Series resistance (3–12 MΩ) was compensated by 95%. Data acquisition was performed using pClamp10 software (Molecular Devices) and tabulated using Excel (Microsoft Corp.). All experiments were conducted at room temperature.

All chemicals were purchased from Sigma-Aldrich, unless otherwise indicated. The external solution contained (in mM) 150 NaCl, 5 HEPES and 0.1 $CaCl_2$, at pH 7.3–7.4. The internal solution contained (mM) 115 NaCl, 10 NaF, 5 HEPES, 5 Na_4BAPTA (Life Technologies), 1 $MgCl_2$, 0.5 $CaCl_2$, and 10 Na_2ATP, pH 7.3–7.4. The osmotic pressure of all solutions was adjusted to 295–300 mOsm with sucrose, if necessary. When spermine was added, internal solution contained 30 μM spermine instead of 10 mM Na_2ATP. For calcium block experiments, external Ca^{2+} was added into 150 mM NaCl to give a final concentration of either 0.3, 1, 2, 5, 10, 20 or 30 mM, except for the highest (108 mM) Ca^{2+} solution that contained only 108 mM $CaCl_2$ (+HEPES) with no added NaCl. For the 108 mM Ca^{2+} solution, pH was balanced using $Ca(OH)_2$.

Concentrated (10×) agonist stock solutions were prepared by dissolving L-glutamate in the appropriate external solution and adjusting the pH to 7.3–7.4 and were stored frozen at −20 °C. Stocks were thawed on the day of the experiment and used to prepare agonist-containing external solutions.

Combined calcium imaging and electrophysiology

Experiments were performed using a Nikon Eclipse inverted microscope. HEK293T/17 cells were plated on 35-mm dishes with a glass coverslip bottom (Ibidi, ref. no. 80136), which were transfected 48 h after plating at low density to avoid cell cluster formation. Cells were transfected 48 h after plating with the same methodology as for in vitro patch-clamp experiments. Furthermore, all groups were cotransfected in with GCaMP6f, a genetically encoded Ca^{2+} indicator[49].

Electrophysiological and imaging experiments were done simultaneously on isolated and transfected cells. Patch-clamp recordings were performed in whole-cell configuration using borosilicate glass pipette (2–5 MΩ). Series resistance (3–12 MΩ) was compensated by 40%. Local agonist application was performed using a homemade flowpipe from theta tubing with a tip diameter of 150–200 μm. External control or agonist solution were applied intermittently to evoke an AMPAR response using a switcher to control solution flow. Imaging was performed selecting the target cell as region of interest and data acquisition was performed using a Evolve 512 Delta camera (Photometrics). The exposure time was set at 10 ms and images were taken every 9 ms. Data acquisition was performed using pClamp10 software (Molecular Devices) for electrophysiological recordings and Micromanager v.1.4 software for imaging. Imaging data were analysed using Image J software. Data were tabulated using Excel (Microsoft Corp.). All experiments were conducted at room temperature.

Ca^{2+} response was measured as the change in the fluorescence signal divided by the total amount of charge (Q_{total}) during a 2-s agonist pulse.

$$\frac{\Delta F_{Ca^{2+}}}{Q_{total}} = \frac{F_{Ca^{2+}Peak} - F_{Ca^{2+}baseline}}{Q_{total}} \quad (1)$$

where $\Delta F_{Ca^{2+}}$ is the fluorescence signal evoked by the Ca^{2+} sensor GCamp6f bound to Ca^{2+} and Q_{total} is the amount of charge defined by the area under the current by:

$$Q = \int_{t_1}^{t_2} I(t)\mathrm{d}t \quad (2)$$

Preparation of ex vivo brain slices

Mice were anaesthetized with isoflurane and immediately decapitated as described previously[31,58]. The cerebellum was rapidly removed from the skull and submerged in ice-cold cutting solution perfused with carbogen gas (95% O_2, 5% CO_2). Cutting solution contained (in mM): 235 sucrose, 2.5 KCl, 1.25 NaH_2PO_4, 28 $NaHCO_3$, 0.5 $CaCl_2$, 7 $MgCl_2$, 28 D-glucose, 1 ascorbic acid, 3 sodium pyruvate (pH 7.4; 305–315 mOsmol l^{-1}). The cerebellum block was fastened to a platform, transferred to the slicing chamber and again submerged in ice-cold cutting solution, bubbled with carbogen throughout the remainder of the procedure. Thin slices of cerebellar vermis (300 μm) were obtained with a vibrating tissue sectioner (Leica VT1200; Leica Instruments). The slices were transferred to oxygenated artificial cerebrospinal fluid (aCSF) and held at room temperature (21–23 °C) for at least 1 h before recordings were performed. aCSF contained the following (in mM): 125 NaCl, 2.5 KCl, 1.25 NaH_2PO_4, 26 $NaHCO_3$, 2 $CaCl_2$, 1 $MgCl_2$, 25 D-glucose (pH of 7.4; 305–315 mOsmol l^{-1}).

Ethical approval

All experiments were performed in accordance with the guidelines of the Canadian Council on Animal Care and were approved by the Animal Care Committee of McGill University (approval no. 2013-7435).

Animals

Wild-type mice with a C57BL/6J background were obtained from Charles River Laboratories and maintained as a breeding colony at McGill University. Both male and female wild-type mice used for the experiments ranged from postnatal days 18 to 30. Animals were permitted ad libitum access to food and water.

Electrophysiological recordings from acutely isolated brain slice tissue

Slice experiments were performed on an Olympus BX51 upright microscope (Olympus) equipped with differential interference contrast and/or infrared optics[31,58]. Recordings were made from either visually identified Purkinje cells or Bergmann glia in acute sagittal slices of cerebellar vermis. Patch pipettes were prepared from thick-walled borosilicate glass (GC150F-10, OD 1.5 mm, ID 0.86 mm; Harvard Apparatus Ltd) and had open tip resistances of 3–6 MΩ when filled with an intracellular recording solution. Internal solution contained (in mM): 140 CsCl, 10 HEPES, 10 EGTA, 2 $MgCl_2$ and 30 μM spermine-HCl to examine rectification due to polyamine channel block (pH of 7.4; 295–305 mOsmol l^{-1}). Local agonist and/or antagonist applications were performed

using a homemade flowpipe from theta tubing with a tip diameter of 300–400 µm. The external solution was the same as described above with the addition of 10 µM D-APV to block *N*-methyl-D-aspartate receptors. Excised membrane patches were placed near the mouth of a double-barrelled flowpipe, which rapidly jumped between control and the solution containing 10 mM L-Glu (250-ms duration). Recordings were performed using a Multiclamp 700 A amplifier (Molecular Devices). The bath was continuously perfused at room temperature (21–23 °C) with aCSF at a rate of 1–2 ml min^{-1}. Currents were filtered at 5 kHz with an eight-pole low-pass Bessel filter (Frequency Devices) and digitized at 25 kHz with a Digidata 1322A data acquisition board and Clampex 10.1 (pClamp) software.

Estimation of the relative Ca^{2+} permeability

AMPAR *I–V* relationships were used to calculate reversal potentials in 150 mM external Na^+ and in 108 mM external Ca^{2+} solutions.

The data were fit with a polynomial function with the order of 4 to estimate the reversal potential where the *x* intercept of the polynomial fit was determined to be the reversal potential (E_{rev}). Ca^{2+} permeability relative to Na^+ (P_{Ca}/P_{Na}) was calculated using the equation[48]:

$$\frac{P_{Ca}}{P_{Na}} = \frac{[Na^+]_i\left(1+e^{\frac{E_{rev(Ca)}F}{RT}}\right)}{4[Ca^{2+}]_o\left(e^{\frac{(E_{rev(Na)}-E_{rev(Ca)})F}{RT}}\right)} \quad (3)$$

where P_{Ca} and P_{Na} are the permeability coefficients for Ca^{2+} and Na^+, respectively, *F* is Faraday's constant, *R* is the gas constant and *T* is the temperature in kelvins.

Measurement of AMPAR channel kinetics

Channel gating kinetics of AMPARs were assessed by applying a 250- or 1-ms application of L-glutamate (10 mM) to measure the peak and steady-state equilibrium response, the rate and extent of desensitization, deactivation and recovery from desensitization kinetics (indicated as off kinetics) (details in Supplementary Table 2). Kinetics were fit using a mono- or bi-exponential function as described previously[34] and presented as weighted means in the case of a bi-exponential function.

Single permeant blocker model for external Ca^{2+} and internal polyamines block

Conductance–voltage (*G–V*) relationships of block by external Ca^{2+} or internal polyamines were fit using Origin Pro 2020 (OriginLab) with the following equation[50]:

$$G = \frac{G_{max}}{1+\frac{[blocker]}{K_d}} \quad (4)$$

where K_d is the dissociation constant at 0 mV defined by:

$$K_d = \frac{k_{off}+k_{perm}}{k_{on}} = \frac{\text{sum of exit rates}}{\text{binding rate}} \quad (5)$$

and redefined according to the equation:

$$K_d = g \times \exp\left(\frac{V}{h}\right) + L \times \exp\left(\frac{V}{k}\right) \quad (6)$$

where *h* and *k* represent the voltage dependence of *g* (k_{off}/k_{on}) and *L* (k_{perm}/k_{on}), respectively.

Inhibition plots of external Ca^{2+} block

Voltage ramps were used to determine the degree of Ca^{2+} block of AMPARs at a range of holding potentials from −100 to +100 mV. Cyclothiazide was added at a final concentration of 100 µM to the control and agonist external solutions to reduce receptor desensitization. Currents recorded in control solution were used to leak-subtract experimental records.

Dose-inhibition curves of external Ca^{2+} block were fit using a single-binding site isotherm function or double-binding site isotherm function as described previously[59]. The single-binding site isotherm function is given by:

$$G = G_0 + \frac{1-G_0}{1+\left(\frac{[Ca]}{IC_{50}}\right)^n} \quad (7)$$

where IC_{50} is the concentration of external Ca^{2+} that elicits half-maximal block (or half-maximum inhibitory concentration), *n* is the slope and G_0 is the steady-state response. The double-binding site isotherm function, on the other hand is given by:

$$G = G_0 + \frac{G_{max}-G_{mid}}{1+\left(\frac{[Ca]}{IC_{50(High)}}\right)^n} + \frac{G_{mid}-G_0}{1+\left(\frac{[Ca]}{IC_{50(Low)}}\right)^n} \quad (8)$$

where $IC_{50\,(High)}$ and $IC_{50\,(Low)}$ are the concentrations of external Ca^{2+} that elicits half-maximal block of the high- and low-affinity components, respectively. G_{mid} is the boundary value between high and low-affinity components.

Primers for single point mutations

To introduce single point mutations, the following reversal and forward primers were used for PCR reactions:

R607E in GluA2Ri

Fwd: 5′–CTCTGGTTTTCCTTGGGTGCCTTTATG**ga**GCAAGGATG CGATATCTCGCCAAGATCCC–3′

Rev: 5′–GGGATCTTGGCGAGATATCGCATCCTTGC**tc**CATAAAGGCA CCCAAGGAAAACCAGAG–3′

R607G in GluA2Ri

Fwd: 5′–CTCTGGTTTTCCTTGGGTGCCTTTATG**g**GGCAAGGATG CGATATCTCGCCAAGATCCC–3′

Rev: 5′–GGGATCTTGGCGAGATATCGCATCCTTGCC**c**CATAAAGGCA CCCAAGGAAAACCAGAG–3′

D611N in GluA2Ri

Fwd: 5′–CTCTGGTTTTCCTTGGGCGCCTTTATGCGGCAAGGAT GC**a**ATATTTCGCCAAGATCCC–3′

Rev: 5′–GGGATCTTGGCGAAATATTGCATCCTTGCCGCATAAAGGC**g** CCCAAGGAAAACCAGAG–3′

A789F in GluA1

Fwd: 5′–CTCAGCAATGTGTTCGGCGTG**ttc**TACATCCTGATTGGA GGGCTGGGGCTAGCCATG–3′

Rev: 5′–CAGCATGGCTAGCCCCAGCCCTCC**aat**CAGGATGTAGA ACACGCCGAAATTGCT–3′

Bold indicates the nucleotide that was introduced to mutate each residue.

Modelling of Ca^{2+} block of AMPARs

Ca^{2+} block was assumed to be caused by Ca^{2+} ions binding to sites within the pore of the AMPARs, and was modelled using a formalism similar to that first described by Woodhull[60]. We examined various numbers and configurations of binding sites that together comprise five separate models (Extended Data Fig. 8a). For a full description, see the Supplementary Information.

In model 1, the probability of block is determined by the occupancy of a single-binding site, B1. This model is identical to that of Woodhull[60] except that the blocking ion (calcium) has a valence of 2.

In model 2, the probability of block is determined by the occupancy of two binding sites. External calcium can bind to a first site (B1) and

then transition to a second site (B2). However, external calcium cannot bind to B2 directly. In this model, block occurs if the second binding site, B2, is occupied by calcium; calcium occupancy of B1 does not directly block the pore.

In model 3, the block is modelled in the same way as model 2, except that the pore is blocked if either binding site, B1 or B2, is occupied by calcium.

In model 4, the block is modelled in the same way as model 2, except that external calcium can also bind directly to the second binding site, B2, thus bypassing the first binding site, B1.

In model 5, the block is modelled the same as model 4, except that the pore is blocked if either binding site, B1 or B2, is occupied by calcium.

Each model was fit to the calcium block data of the various AMPARs across all voltage simultaneously by minimizing the sum of square errors. The most parsimonious model was selected based on the Bayesian information criterion[61]. After concluding that Model 4 best explained the AMPAR blocking data (Main Text and Extended Data Fig. 8), we analysed the voltage sensitivity of each calcium binding site in more detail. To do so, we investigated four nested models based on model 4 that progressively restrict the voltage dependence of calcium binding to sites B1 and B2 (Extended Data Fig. 9a–e and Supplementary Information). We compared the goodness of fits of the increasingly restricted models using multiple *F*-tests with a Bonferroni corrected significance threshold of 0.05 (Extended Data Fig. 9f). Uncertainty in parameter estimates was calculated by repeatedly fitting the model to bootstrap samples[62] of the data (Extended Data Fig. 10).

Reporting summary

Further information on research design is available in the Nature Portfolio Reporting Summary linked to this article.

Data availability

Data supporting the findings of this study are available upon request. The referred protein structure has the Protein Data bank (PDB) accession code 7OCA. Supplementary Information is available for this paper. The data obtained to create Extended Data Fig. 1c have been taken from refs. 16,31,34. Source data are provided with this paper.

Code availability

Code used in the current study is publicly available on GitHub (https://github.com/niklasbrake/AMPAR_permeation_modelling).

56. Brown, P. M., Aurousseau, M. R., Musgaard, M., Biggin, P. C. & Bowie, D. Kainate receptor pore-forming and auxiliary subunits regulate channel block by a novel mechanism. *J. Physiol.* **594**, 1821–1840 (2016).
57. Bowie, D., Garcia, E. P., Marshall, J., Traynelis, S. F. & Lange, G. D. Allosteric regulation and spatial distribution of kainate receptors bound to ancillary proteins. *J. Physiol.* **547**, 373–385 (2003).
58. Alexander, R. P. D. & Bowie, D. Intrinsic plasticity of cerebellar stellate cells is mediated by NMDA receptor regulation of voltage-gated Na(+) channels. *J. Physiol.* **599**, 647–665 (2021).
59. Wong, A. Y., Fay, A. M. & Bowie, D. External ions are coactivators of kainate receptors. *J. Neurosci.* **26**, 5750–5755 (2006).
60. Woodhull, A. M. Ionic blockage of sodium channels in nerve. *J. Gen. Physiol.* **61**, 687–708 (1973).
61. Konishi, S. & Kitagawa, G. *Information Criteria and Statistical Modeling* (Springer, 2008).
62. Efron, B. & Tibshirani, R. *An Introduction to the Bootstrap* (Chapman and Hall, 1993).

Acknowledgements We thank former Bowie laboratory members, D. MacLean (University of Rochester), P. Brown (University of Cologne), M. Aurousseau and H. McGuire for their preliminary experiments on this project and current laboratory members for their feedback on the manuscript, especially C. Koens. We also thank T. Nakagawa (Vanderbilt) for fruitful and interesting discussions about Ca^{2+} permeation and I. Greger (LMB) for providing the tethered TARP-γ8 complementary DNA. We thank S. Bosse (Delta Phototonics) for his technical support with the imaging system. The work was supported by finance from the Canadian Institutes of Health Research (grant on. FRN 163317, D.B.), and from the Natural Sciences and Engineering Research Council of Canada (Discovery Grant, A.K.). A.M.P and R.P.D.A. were supported by the Natural Sciences and Engineering Research Council of Canada. Y.Y. was supported by Fonds de recherche du Québec-Santé (FRQS). N.B. was supported by Fonds de recherche du Québec-Nature et technologies. X-T.W. was supported by a studentship from the Integrated Program in Neuroscience at McGill University.

Author contributions F.M.-C., X.-t.W. and Y.Y. conducted recombinant electrophysiology experiments and analysed data and contributed equally. N.B. contributed to the computational modelling. R.P.D.A. conducted the native electrophysiology experiments and analysed data. A.M.P. generated figures, edited the manuscript and was involved in the discussions. A.K. supervised and provided insights into the computational modelling. D.B. conceived the project, supervised all the experiments, wrote the manuscript and provided financial support.

Competing interests The authors declare no competing interests.

Additional information
Supplementary information The online version contains supplementary material available at https://doi.org/10.1038/s41586-025-08736-2.

Correspondence and requests for materials should be addressed to Derek Bowie.

Peer review information *Nature* thanks Albert Lau and the other, anonymous, reviewer(s) for their contribution to the peer review of this work. Peer reviewer reports are available.

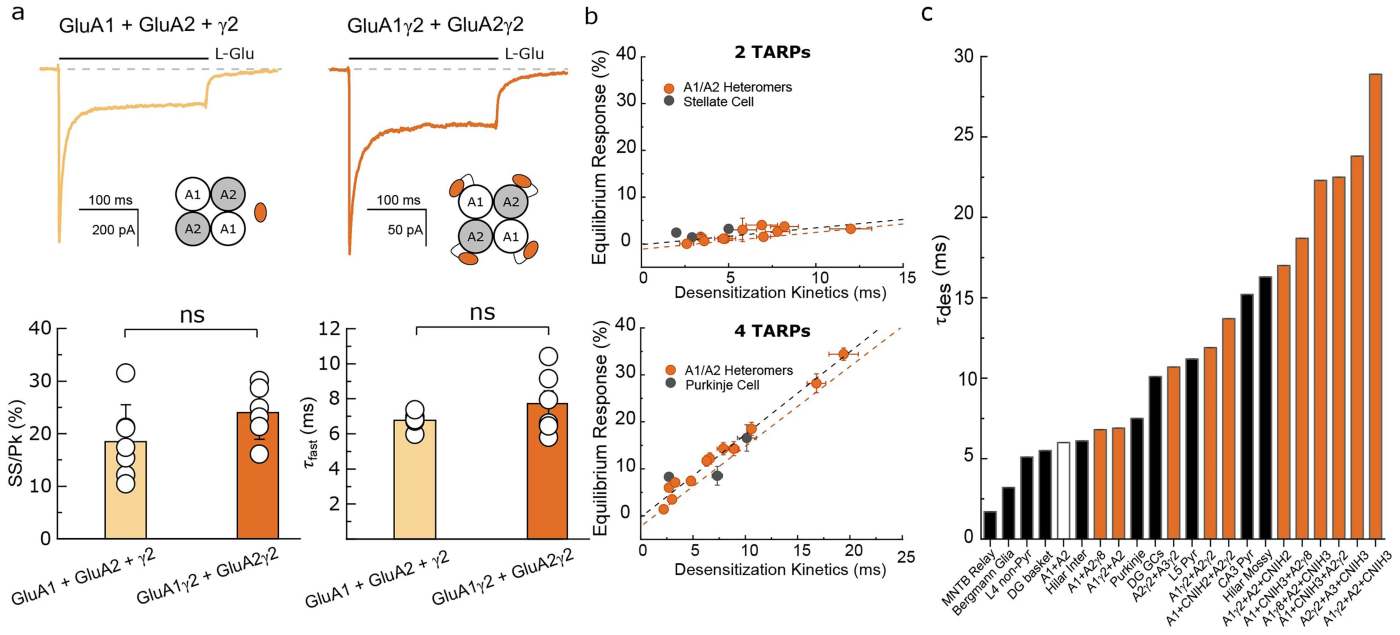

Extended Data Fig. 1 | AMPARs with tethered TARP auxiliary subunits faithfully reproduce the gating behaviour of native AMPARs. a. (Upper) Example electrophysiological records of L-Glu responses (10 mM) of GluA1/A2 AMPAR heteromers co-expressed with (left) or tethered to (right) TARP γ2. (Lower) Statistical analyses of the degree of AMPAR desensitization (left, SS/Pk) or rate of onset of desensitization (right, τ_{fast}) reveals that the gating properties are indistinguishable when co-expressed with or tethered to TARP γ2. (Adapted from Perozzo et al., 2023). **b**. Plots comparing the gating properties of recombinant A1/A2 heteromers (orange symbol) and native (black symbol) AMPARs expressed by inhibitory stellate (upper) and Purkinje (lower) cells from the cerebellum. In both cases, recombinant AMPARs were expressed as fusion proteins with TARP γ2 tethered to either GluA1 or GluA2 subunit (upper) or to both (lower). Importantly, the desensitization properties of recombinant receptor exactly matched with functional behavior of stellate cells when only two TARP γ2 subunits were present (upper) whereas the Purkinje cell data was exactly matched by recombinant data where all four AMPAR subunits were tethered to TARP γ2. (Adapted from Perozzo et al., 2023). **c**. Desensitization rates (τ_{des}) of native and recombinant AMPARs arranged in ascending order shows that they form a continuum of functional behavior. Values for native data were taken from Geiger et al.[16] and Dawe et al.[31] and the values for the recombinant were taken from this study. The black bars correspond to AMPAR heteromers that are tethered to at least two TARP subunits whereas the unfilled bar corresponds to GluA1/A2 heteromers lacking TARPs.

AMPARs+TARPs

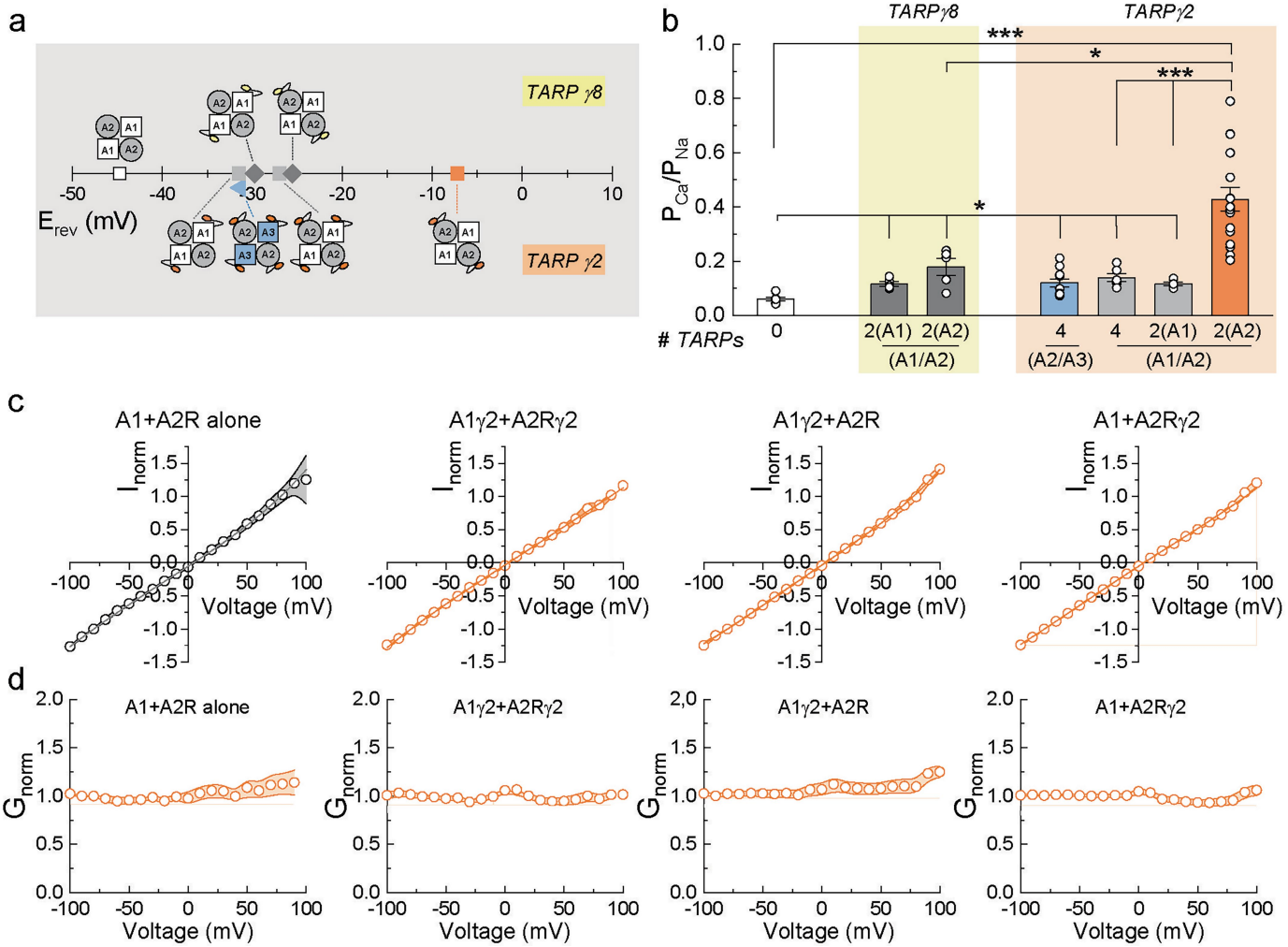

Extended Data Fig. 2 | TARPs promote Ca^{2+} permeability of GluA2-containing AMPARs while remaining polyamine insensitive. a. Different AMPAR-TARP complexes arranged according to the reversal potential observed in 108 mM external Ca^{2+} solution (A1/A2: $E_{rev}Ca^{2+}$ = −44.8 ± 2.8 mV, n = 6; A1γ8/A2: $E_{rev}Ca^{2+}$ = −29.7 ± 1.8 mV, n = 5; A1/A2γ8: $E_{rev}Ca^{2+}$ = −25.6 ± 2.9 mV, n = 5; A2γ2/A3γ2: $E_{rev}Ca^{2+}$ = −31.4 ± 2.3 mV, n = 11; A1γ2/A2: $E_{rev}Ca^{2+}$ = −31.5 ± 1.2 mV, n = 5; A1/A2γ2: $E_{rev}Ca^{2+}$ = −7.2 ± 1.8 mV, n = 16; A1γ2/A2γ2: $E_{rev}Ca^{2+}$ = −27.0 ± 1.8 mV, n = 6). **b.** Pooled data of P_{Ca}/P_{Na} of AMPAR-TARP complexes co-assembled with TARP γ2 or γ 8 (A1/A2 P_{Ca}/P_{Na} = 0.06 ± 0.01, n = 6; A1γ8/A2 P_{Ca}/P_{Na} = 0.12 ± 0.01, n = 5; A1/A2γ8 P_{Ca}/P_{Na} = 0.18 ± 0.03, n = 5; A2γ2/A3γ2 P_{Ca}/P_{Na} = 0.12 ± 0.01, n = 11; A1γ2/A2 P_{Ca}/P_{Na} = 0.12 ± 0.01, n = 5; A1/A2γ2 P_{Ca}/P_{Na} = 0.43 ± 0.04, n = 16; A1γ2/A2γ2 P_{Ca}/P_{Na} = 0.14 ± 0.01, n = 6). Two-sided Kruskal-Wallis ANOVA followed by Mann-Whitney *U* tests with Bonferroni-Holmes correction. *p*-value * <0.05, ** <0.01, *** <0.001. **c.** IV plots of different AMPAR-TARP complexes in external 150 mM Na^+ (open circles fitted by a 4th order polynomial function) solution. **d.** GV plots of AMPAR-TARP complexes obtained from IV curves above (c). Open circles show average normalized response and colored shading show s.e.m. (A1/A2: n = 6; A1γ2/A2: n = 5; A1/A2γ2: n = 16; A1γ2/A2γ2: n = 6).

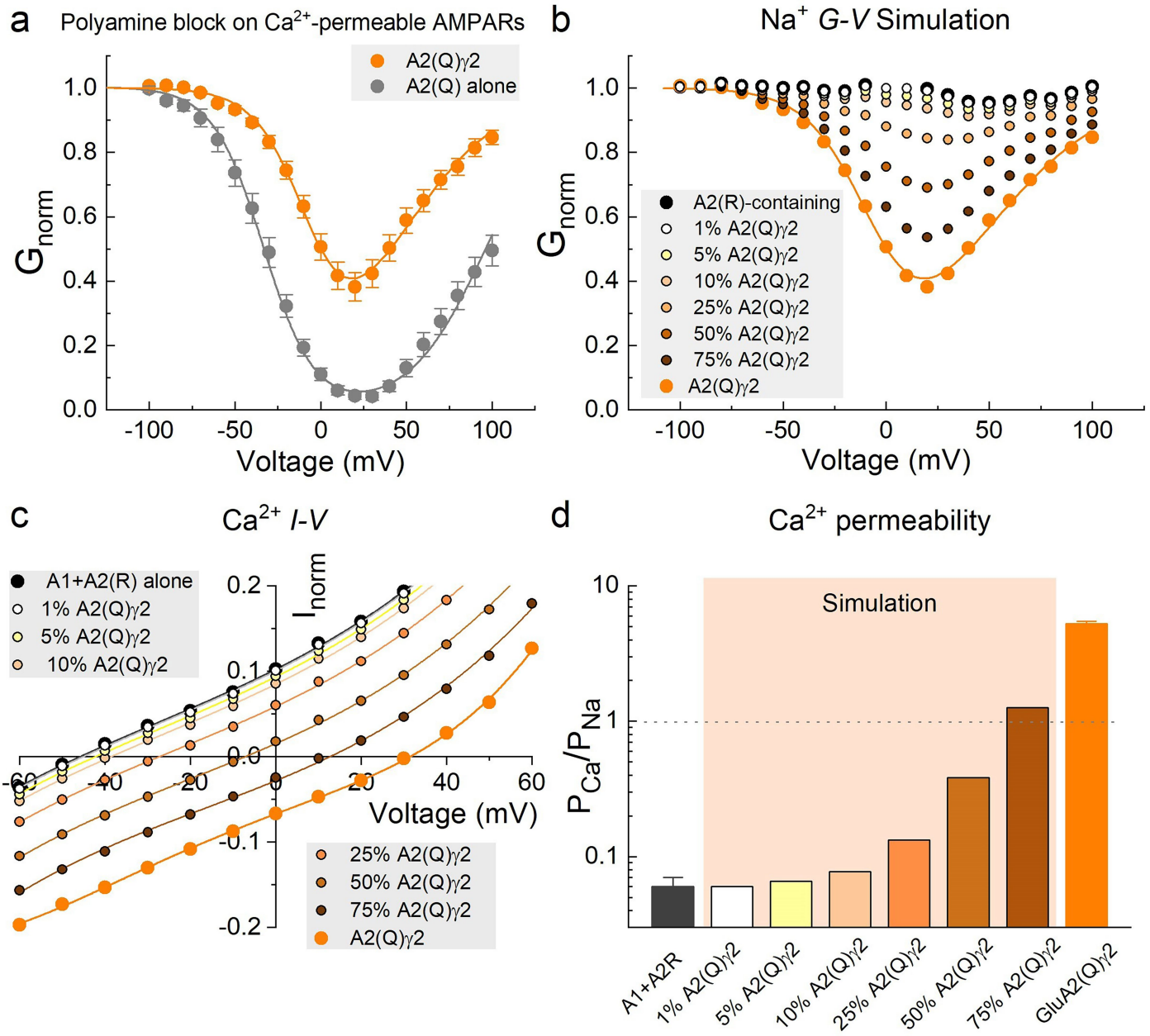

Extended Data Fig. 3 | Simulations of current-voltage (IV) and conductance-voltage (GV) plots establishes that data from edited GluA2-containing AMPARs is not impacted by unedited AMPARs. a. GV plots of unedited GluA2(Q) AMPARs showing that tethering TARP γ2 significantly attenuates the degree of block by cytoplasmic spermine (30 μM). Adapted from the data shown in Supplementary Table 3. **b**. A series of GV plots where the contribution (%) of unedited AMPARs to the overall AMPAR response is reduced in a stepwise manner. Note that shape of the GV plot with only 1 % contribution of unedited AMPARs best fits the data we have observed with GluA1/A2 heteromers. **c**. A series of Ca^{2+} IV plots where the contribution (%) of unedited AMPARs to the overall AMPAR response was adjusted in an incremental manner. Note, that at least 50% of unedited AMPARs would be needed for the reversal potential to be in the positive voltage range. **d**. The relative Ca^{2+} permeability of AMPARs estimated from the simulated Ca^{2+} IV plot data shown in c. Note, that for the relative Ca^{2+} permeability to be close to 1 (dotted line), as described for GluA1/A2 heteromers with TARP γ2 and CNIH3, almost 75 % of the overall response would need to contain unedited AMPARs.

AMPARs+TARPs+CNIHs

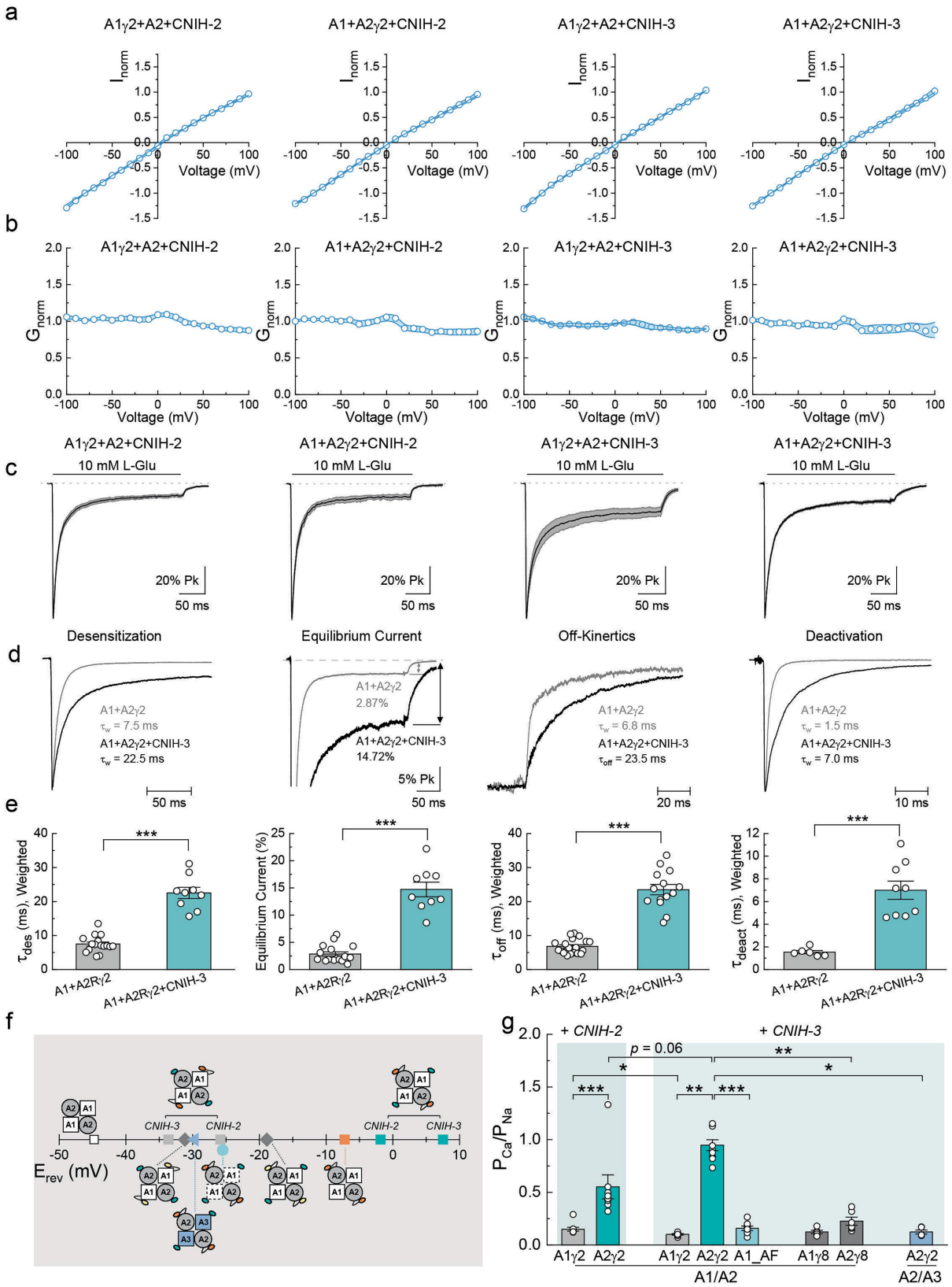

Extended Data Fig. 4 | See next page for caption.

Extended Data Fig. 4 | Current-voltage (IV) and conductance-voltage (GV) plots confirm that GluA2-containing AMPARs are polyamine insensitive and kinetic properties corroborate CNIH presence in the AMPAR complex. **a**. IV plots of different AMPAR-TARP + CNIH complexes in external 150 mM Na^+ (open circles fitted by a 4th order polynomial function) solution. **b**. GV plots of the AMPAR-TARP complexes obtained from IV curves above (a). Open circles show average normalized response and colored shading show se.m. (A1γ2/A2 + CNIH-2: n = 9; A1/A2γ2 + CNIH-2: n = 8; A1γ2/A2 + CNIH-3: n = 6; A1/A2γ2 + CNIH-3: n = 9). **c**. Example membrane currents evoked by 10 mM L-Glu (250 ms duration) on GluA1/A2 AMPARs co-assembled with either TARP γ2 and CNIH2 or TARP γ2 and CNH3 (**c**). The grey shadow shows the SEM of the response. **d**. Comparison of gating properties between A1/A2γ2 (in grey) vs A1/A2γ2 + CNIH-3 (black) receptors. **e**. CNIH-3 slows desensitization kinetics of A1/A2γ2 receptors (A1/A2γ2: τ_{des} = 7.5 ± 0.6 ms, n = 16; A1/A2γ2 + CNIH-3: τ_{des} = 22.5 ± 1.7 ms, n = 9). Equilibrium current was enhanced by CNIH-3 (A1/A2γ2: Equilibrium current = 2.9 ± 0.4 %, n = 16; A1/A2γ2 + CNIH-3: Equilibrium current = 14.7 ± 1.3 %, n = 9). CNIH-3 also slowed the off-kinetics of AMPARs (A1/A2γ2: τ_{off} = 6.8 ± 0.5 ms, n = 19; A1/A2γ2 + CNIH-3: τ_{off} = 23.5 ± 1.5 ms, n = 14) and the deactivation kinetics (A1/A2γ2: τ_{deact} = 1.5 ± 0.1 ms, n = 6; A1/A2γ2 + CNIH-3: τ_{deact} = 7.0 ± 0.8 ms, n = 9). Two-sided unpaired t-tests with Welch correction. *p*-value *** <0.001. **f**. AMPAR-TARP + CNIH complexes arranged by the reversal potential observed in 108 mM external Ca^{2+} solution (A1/A2: $E_{rev}Ca^{2+}$ = −44.8 ± 2.8 mV, n = 6; A1γ2/A2 + CNIH-3: $E_{rev}Ca^{2+}$ = −33.6 ± 1.7 mV, n = 6; A1γ2/A2 + CNIH-2: $E_{rev}Ca^{2+}$ = −25.8 ± 2.2 mV, n = 9; A2γ2/A3 + CNIH-3: $E_{rev}Ca^{2+}$ = −29.7 ± 2.2 mV, n = 5; A1γ8/A2 + CNIH-3: $E_{rev}Ca^{2+}$ = −31.2 ± 2.7 mV, n = 5; A1/A2γ8 + CNIH-3: $E_{rev}Ca^{2+}$ = −18.9 ± 3.4 mV, n = 6). Orange square shows the A1/A2γ2 AMPAR to highlight changes in the Ca^{2+} reversal potential induced by CNIH-2 and -3 auxiliary proteins (cyan squares, A1/A2γ2 + CNIH-2: $E_{rev}Ca^{2+}$ = −1.8 ± 2.5 mV, n = 8; A1/A2γ2 + CNIH-3: $E_{rev}Ca^{2+}$ = 7.5 ± 1.1 mV, n = 9). Sky-blue circle denotes A1/A2γ2 + CNIH-3 with the A789F mutation which left-shifts the Ca^{2+} reversal potential ($A1_{AF}$/A2γ2 + CNIH-3: $E_{rev}Ca^{2+}$ = −25.5 ± 3.1 mV, n = 8). **g**. Pooled data of P_{Ca}/P_{Na} from the AMPAR complexes shown in (f) grouped by CNIH and TARP type (A1γ2/A2 + CNIH-2: P_{Ca}/P_{Na} = 0.15 ± 0.02, n = 9; A1/A2γ2 + CNIH-2: P_{Ca}/P_{Na} = 0.55 ± 0.11, n = 8; A1γ2/A2 + CNIH-3: P_{Ca}/P_{Na} = 0.10 ± 0.01, n = 6; A1/A2γ2 + CNIH-3: P_{Ca}/P_{Na} = 0.95 ± 0.05, n = 9; $A1_{AF}$/A2γ2 + CNIH-3: P_{Ca}/P_{Na} = 0.16 ± 0.02, n = 8; A1γ8/A2 + CNIH-3: P_{Ca}/P_{Na} = 0.12 ± 0.02, n = 5; A1/A2γ8 + CNIH-3: P_{Ca}/P_{Na} = 0.23 ± 0.04, n = 6; A2γ2/A3 + CNIH-3: P_{Ca}/P_{Na} = 0.12 ± 0.02, n = 5). Two-sided Kruskal-Wallis ANOVA followed by Mann-Whitney *U* tests with Bonferroni-Holmes correction. *p*-value * <0.05, ** <0.01, *** <0.001.

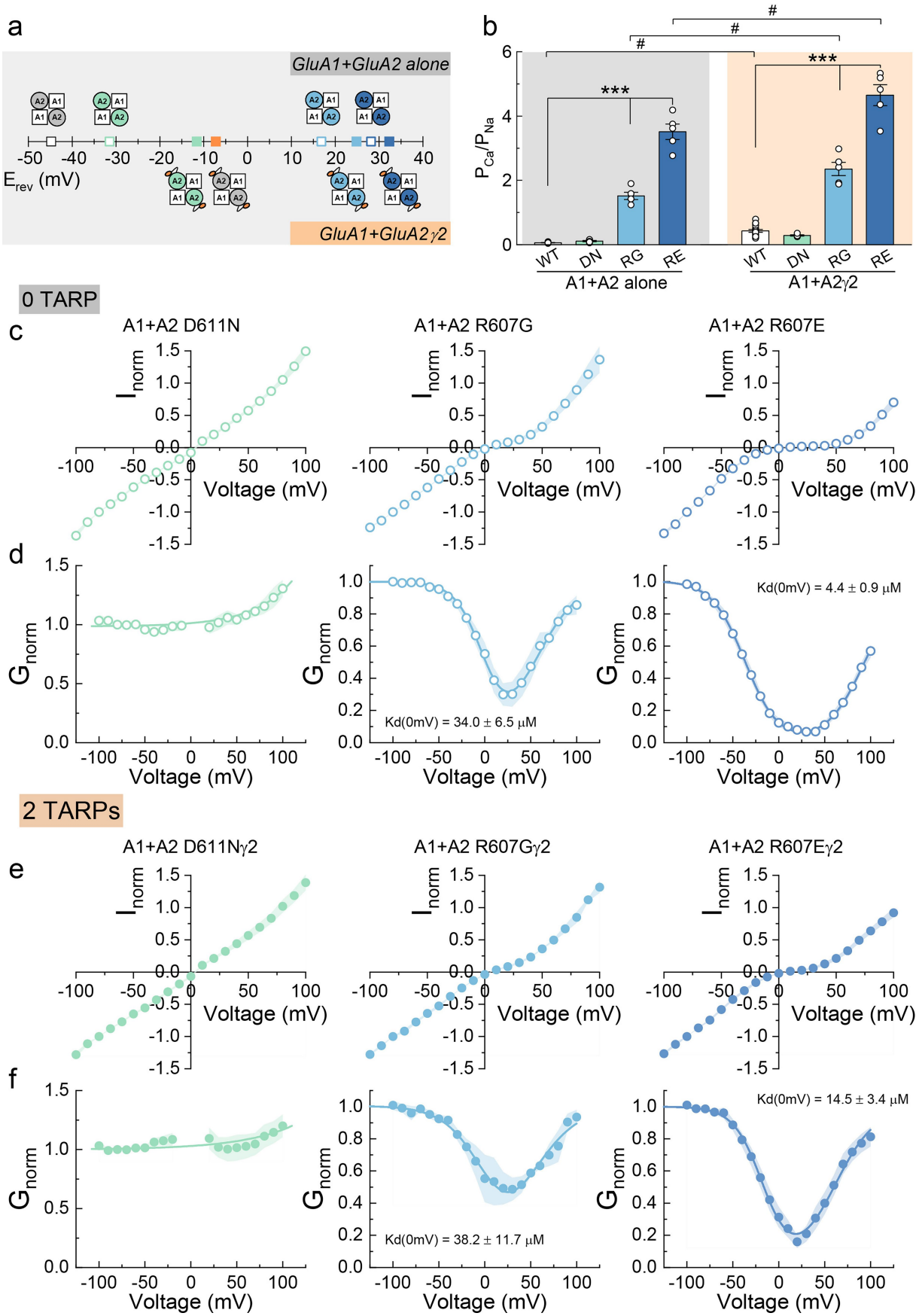

Extended Data Fig. 5 | See next page for caption.

Extended Data Fig. 5 | TARP γ2 increases the Ca^{2+} permeability of missense mutations. a. The Ca^{2+} reversal potential shift with the GluA2 missense mutations (D611N in green, R607G in light blue and R607E in dark blue) in the absence and presence of TARP γ2. **b**. The Na^{+}-relative Ca^{2+} permeability of GluA1+ GluA2 missense mutations (D611N in green, R607G in light blue and R607E in dark blue) in the absence and presence of TARP γ2. Two-sided two-way between-subject ANOVA was performed upon the dataset, decomposing with Tukey's HSD post hoc analysis respectively. #: $p < 0.05$; ***: $p < 0.001$. **c**. IV plots of GluA2-containing AMPARs mutated at the pore region (D611N) and the pore selectivity filter (R607G and R607E). **d**. GV plots obtained from IV curves above (c). A1 + $A2_{D611N}$ channels exhibit a linear GV relationship while A1 + $A2_{R607G}$ and A1 + $A2_{R607E}$ GV curves show block by internal spermine (A1 + $A2_{R607G}$ $Kd_{(0\,mV)}$ = 34 ± 6.5 μM n = 4 and A1 + $A2_{R607E}$ $Kd_{(0\,mV)}$ = 4.4 ± 0.9 μM n = 5). Open circles show average normalized response, colored shading show se.m., and the solid red line corresponds to the fit of a single permeant blocker model. **e**. IV plots of different A1/A2γ2 AMPARs mutated at the +4 site (D611N) and selectivity filter (R607G and R607E). **f**. GV plots obtained from IV curves above (e). A1/A2$γ2_{D611N}$ channels show a linear GV relationship while A1/A2$γ2_{R607G}$ and A1/A2$γ2_{R607E}$ GV curves show sensitivity to block by internal spermine (A1/A2$γ2_{R607G}$ $Kd_{(0\,mV)}$ = 38.2 ± 11.7 μM n = 5 and A1/A2$γ2_{R607E}$ $Kd_{(0\,mV)}$ = 14.5 ± 3.4 μM n = 7). Open circles show average normalized response, colored shading show s.e.m., and the solid redline denotes fits using a single permeant blocker model.

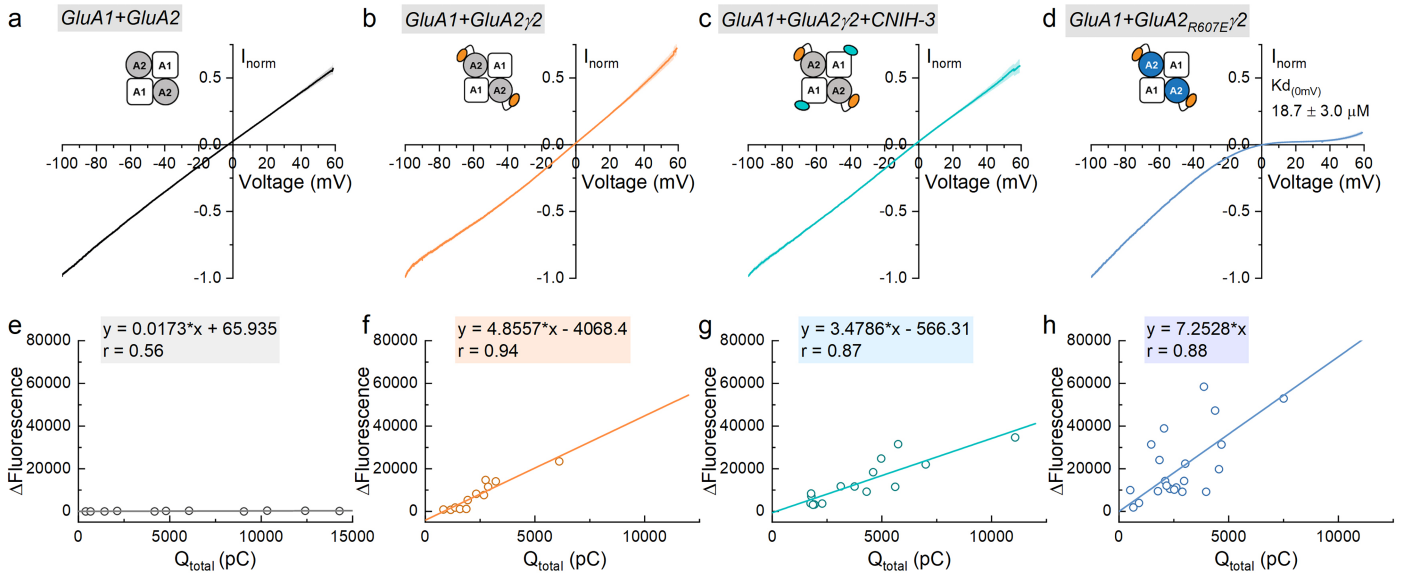

Extended Data Fig. 6 | Current-voltage (I-V) plots from whole-cell recording and Linear regression relationships between Ca^{2+} induced fluorescent intensity (ΔFluorescence) and total charge transfer (Q_{total}) of whole-cell current recording. a-d show the I-V relationships recorded using a RAMP protocol, from −100mV to +60 mV, with whole-cell configuration for GluA1/A2 (black, n = 11), GluA1/A2γ2 (orange, n = 12), GluA1/A2γ2/CNIH-3 (cyan, n = 15) and GluA1/$A2_{R607E}$γ2 (dark blue, n = 12), respectively. The shades of each I-V plot indicates the SEM. Noted that GluA1/$A2_{R607E}$γ2 receptors are sensitive to internal polyamines with an affinity of $Kd_{(0mV)}$ value of 18.7 ± 3.0 μM. **e-h** show the linear regression relationships between Ca^{2+} induced fluorescent intensity (ΔFluorescence) and total charge transfer (Q_{total}) of whole-cell current recording for GluA1/A2 (grey, n = 11), GluA1/A2γ2 (orange, n = 12), GluA1/A2γ2/CNIH-3 (cyan, n = 15) and GluA1/$A2_{R607E}$γ2 (dark blue, n = 12), respectively. Scatters indicate individual data points, while the solid lines are the linear regression for each group: GluA1/A2: y = 0.0173*x + 65.935, r = 0.56; GluA1/A2γ2: y = 4.8557*x-4068.4, r = 0.94; GluA1/A2γ2/CNIH-3: y = 3.4786*x-566.31, r = 0.87 and GluA1/$A2_{R607E}$γ2: y = 7.2528*x, r = 0.88.

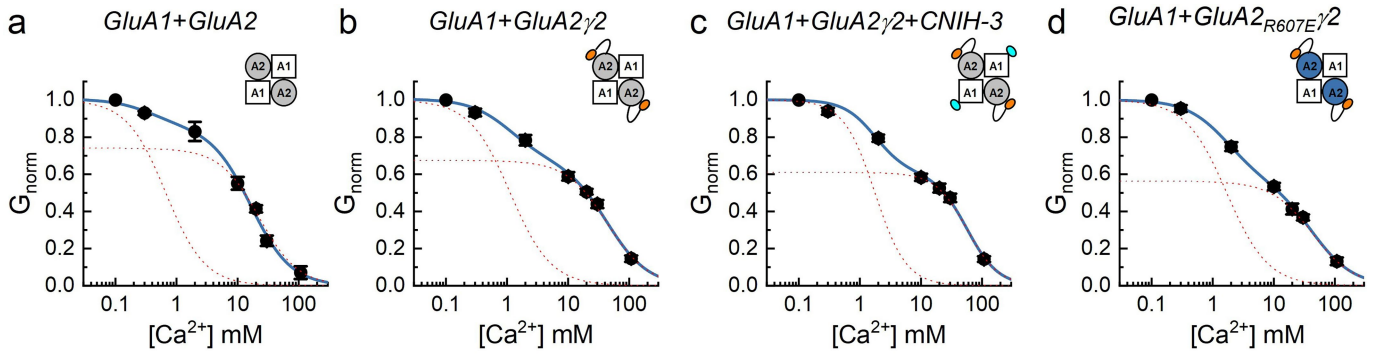

IC_{50} (high) = 0.67 mM	IC_{50} (high) = 1.13 mM	IC_{50} (high) = 1.77 mM	IC_{50} (high) = 1.70 mM
IC_{50} (low) = 22.41 mM (74%)	IC_{50} (low) = 43.84 mM (67%)	IC_{50} (low) = 56.86 mM (61%)	IC_{50} (low) = 43.14 mM (56%)

Extended Data Fig. 7 | Ca^{2+} block of GluA2-containing AMPARs at two binding sites. Fits of two binding site isotherm to Ca^{2+} inhibition data recorded at −100 mV of AMPARs composed of **a**. GluA1/A2 (n = 7), **b**. GluA1/A2-γ2 (n = 16), **c**. GluA1+CNIH−3/A2-γ2 (n = 9) and **d**. GluA1/A2-γ2 R607E (n = 8). The solid line corresponds to the sum of the two binding site isotherm and the dotted lines are the individual isotherm fits.

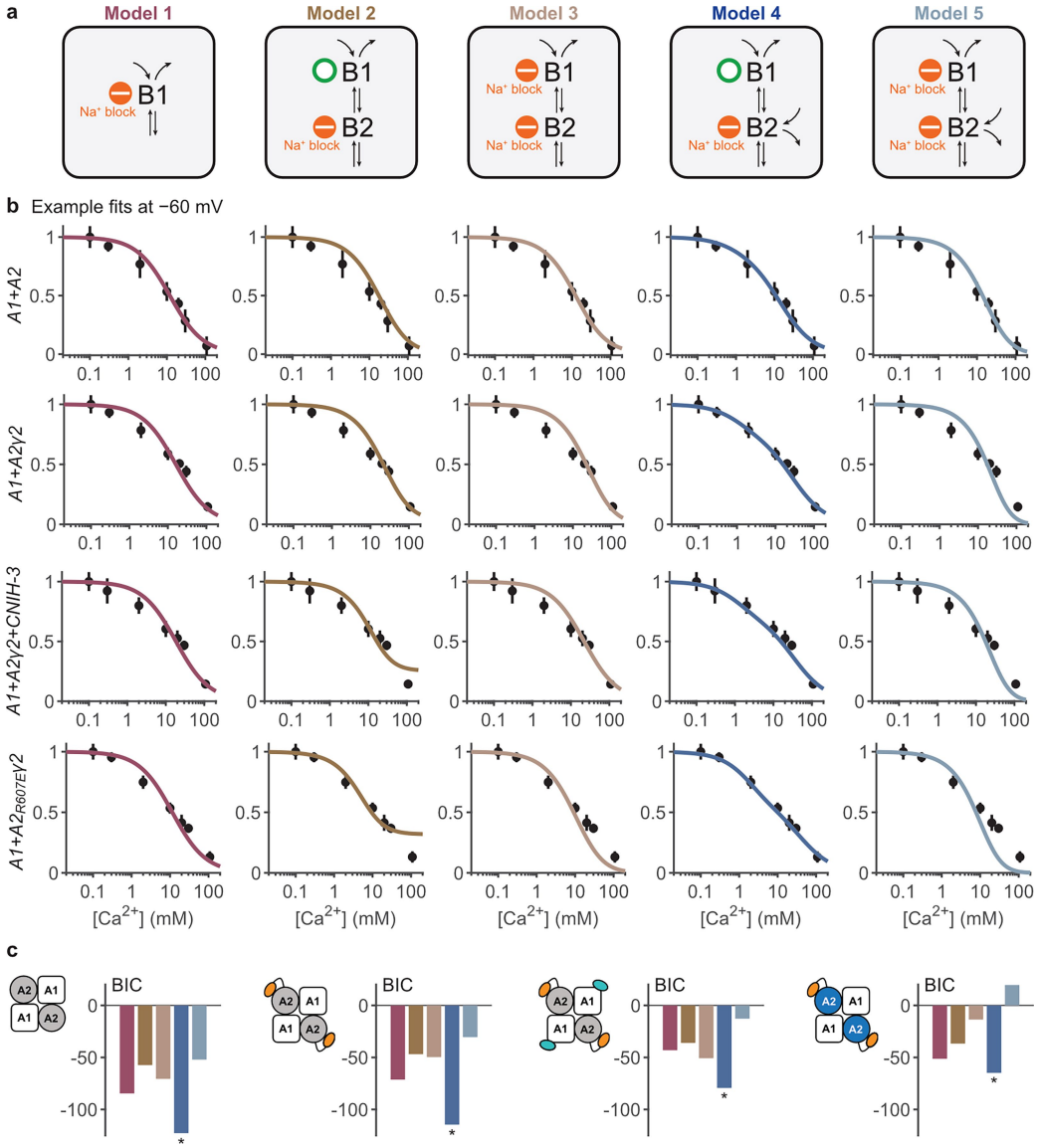

Extended Data Fig. 8 | A two-binding site permeation model best captures voltage-dependent calcium block of AMPARs. a. Schematic illustrations of the five Ca^{2+} binding models studied. **b**. The black dots are the calcium-dependent G_{norm} values at −60 mV for each AMPAR (top to bottom). The colored lines are the fits for the five models (left to right). G_{norm} is modelled as one minus the probability of calcium binding to site B2 (except model 1, where block is modelled based on calcium binding to site B1). Notice that all the models either overestimate block at low calcium concentration or underestimate block at high calcium concentrations, except for Model 4. **c**. Bayesian information criterion (BIC) computed for each model and AMPAR. Model 4 exhibited the lowest BIC across all AMPARs, indicating that the model is the best trade-off between high accuracy and low complexity.

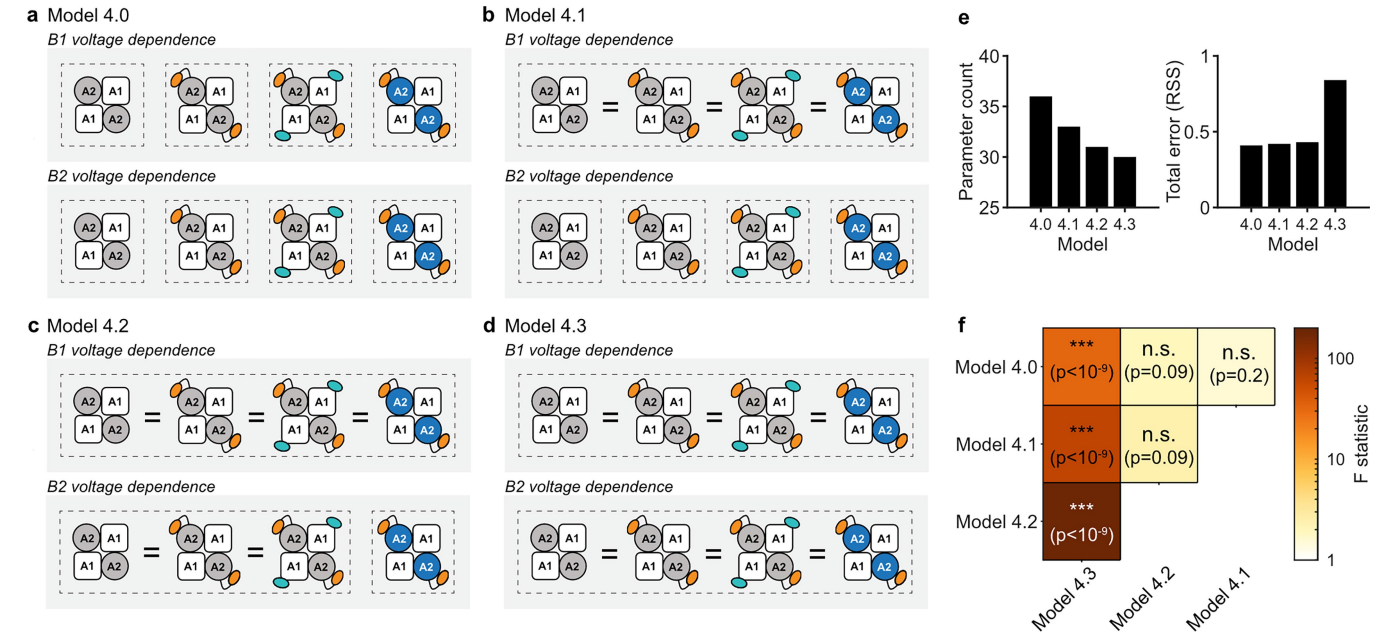

Extended Data Fig. 9 | Nested model comparison identifies similarity in voltage sensitivity among AMPARs (see Supplementary Information). **a**. Illustration of Model 4.0. The voltage dependences of both sites B1 and B2 are allowed to vary among all the AMPAR complexes. Model 4.0 is identical to Model 4. **b**. Illustration of Model 4.1. The voltage dependence of site B2 is allowed to vary among all the AMPAR complexes, but the voltage dependence of site B1 (δ_1) is identical among all AMPARs. **c**. Illustration of Model 4.2. The voltage dependence of site B2 (δ_3) of A1 + A2R607Eγ2 is allowed to vary, but the other AMPARs have identical voltage dependence. **d**. Illustration of Model 4.3. The voltage dependence of all AMPARs are identical. **e**. The number of unique parameters and the residual squared error (RSS) after fitting each of the nested models. **f**. Results of F-tests for model comparison. Models 4.0, 4.1, and 4.2 all performed significantly better than Model 4.3. However, Models 4.0, 4.1, and 4.2 achieved statistically indistinguishable ($p > 0.05$) fits to the data when taking the number of model parameters into account.

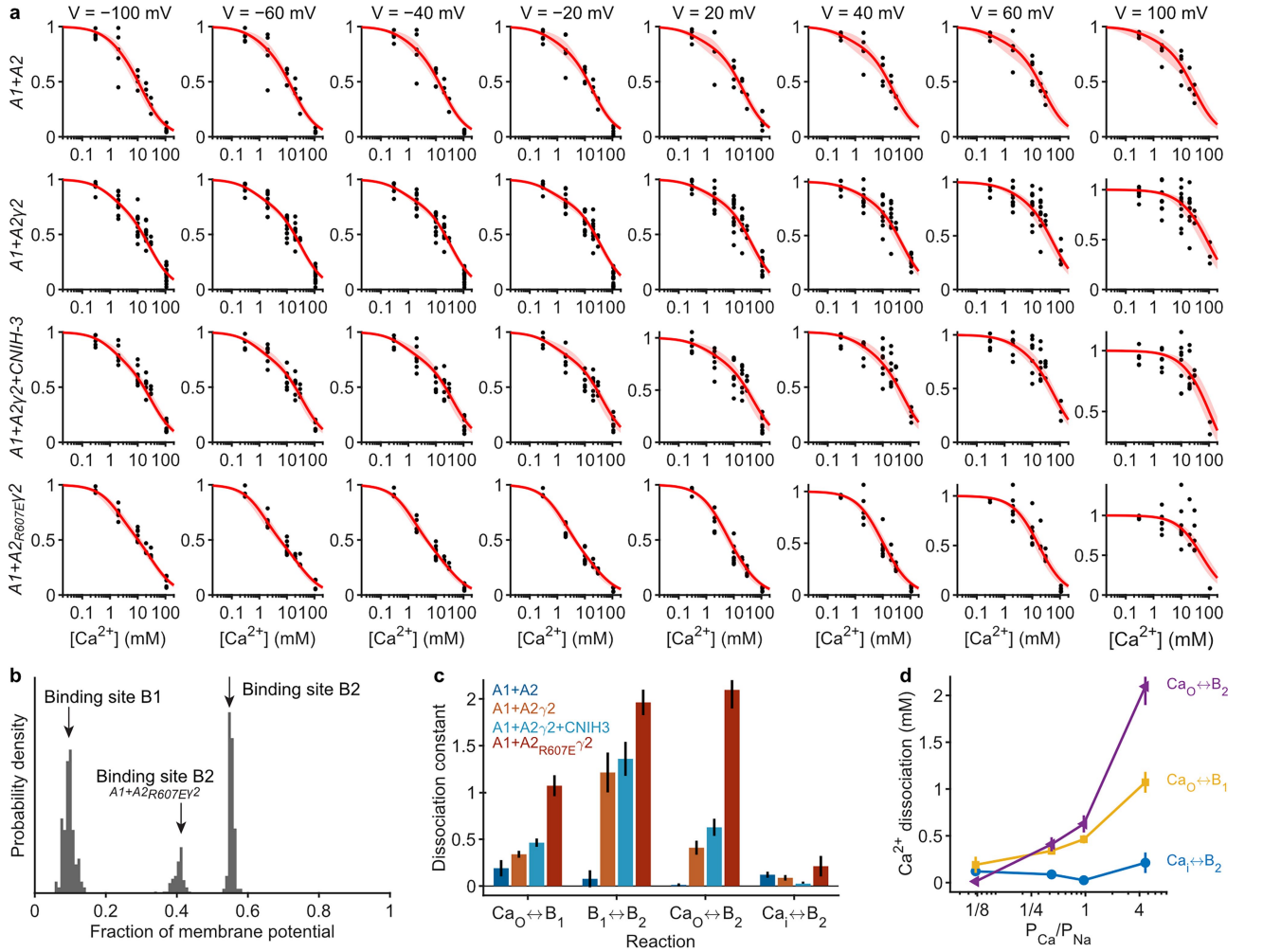

Extended Data Fig. 10 | Calcium block data of A1_A2, A1_A2γ2, and A1_A2γ2 + CIHN3 captured by permeation model (Model 4.2) with identical voltage dependences. a. Black dots indicate normalized AMPAR conductance at various calcium concentrations for four different AMPAR complexes (top to bottom) and various voltages (left to right). The red lines show the fit of Model 4.2. Shading indicates 95% confidence interval of model fit (bootstrap, n = 100). **b**. Optimal parameter values for the voltage dependence of site B1 (δ_1) and site B2 (δ_3) after repeatedly fitting Model 4.2 to 100 bootstrap samples of the data. The voltage dependence of B2 was allowed to differ for GluA1+GluA2R607Eγ2. Notice the second peak in density for the voltage dependence of binding site B2, indicating that in the mutant receptor, binding site B2 sits more shallowly in the membrane electric field compared to the other AMPARs studied. **c**. Dissociation constants of each of the four transitions in Model 4.2 after fitting to each of the four AMPAR complexes. Vertical lines reflect 95% confidence interval (bootstrap, n = 100). **d**. Dissociation constants of calcium binding, same as panel c, now plotted against the calcium permeability of each AMPAR. The dissociation constants are positively associated with calcium permeability for CaO↔B1 ($\rho = 0.95$, spearman correlation, $p < 10\text{-}9$), CaO↔B2 ($\rho = 0.96$, $p < 10\text{-}9$), but not for Cai↔B2 ($\rho = 0.08$, $p = 0.09$).

nature portfolio

Corresponding author(s): Dr. Derek Bowie

Last updated by author(s): Jan 10, 2025

Reporting Summary

Nature Portfolio wishes to improve the reproducibility of the work that we publish. This form provides structure for consistency and transparency in reporting. For further information on Nature Portfolio policies, see our Editorial Policies and the Editorial Policy Checklist.

Statistics

For all statistical analyses, confirm that the following items are present in the figure legend, table legend, main text, or Methods section.

n/a	Confirmed
☐	☒ The exact sample size (*n*) for each experimental group/condition, given as a discrete number and unit of measurement
☐	☒ A statement on whether measurements were taken from distinct samples or whether the same sample was measured repeatedly
☐	☒ The statistical test(s) used AND whether they are one- or two-sided *Only common tests should be described solely by name; describe more complex techniques in the Methods section.*
☒	☐ A description of all covariates tested
☒	☐ A description of any assumptions or corrections, such as tests of normality and adjustment for multiple comparisons
☒	☐ A full description of the statistical parameters including central tendency (e.g. means) or other basic estimates (e.g. regression coefficient) AND variation (e.g. standard deviation) or associated estimates of uncertainty (e.g. confidence intervals)
☒	☐ For null hypothesis testing, the test statistic (e.g. *F*, *t*, *r*) with confidence intervals, effect sizes, degrees of freedom and *P* value noted *Give P values as exact values whenever suitable.*
☒	☐ For Bayesian analysis, information on the choice of priors and Markov chain Monte Carlo settings
☒	☐ For hierarchical and complex designs, identification of the appropriate level for tests and full reporting of outcomes
☒	☐ Estimates of effect sizes (e.g. Cohen's *d*, Pearson's *r*), indicating how they were calculated

Our web collection on statistics for biologists contains articles on many of the points above.

Software and code

Policy information about availability of computer code

Data collection	pClamp10 software (Molecular Devices, LLC), Micromanager 1.4
Data analysis	Origin 2020 (OriginLab), Clampfit 10.5, Image J

For manuscripts utilizing custom algorithms or software that are central to the research but not yet described in published literature, software must be made available to editors and reviewers. We strongly encourage code deposition in a community repository (e.g. GitHub). See the Nature Portfolio guidelines for submitting code & software for further information.

Data

Policy information about availability of data

All manuscripts must include a data availability statement. This statement should provide the following information, where applicable:

- Accession codes, unique identifiers, or web links for publicly available datasets
- A description of any restrictions on data availability
- For clinical datasets or third party data, please ensure that the statement adheres to our policy

Data supporting the findings of the current study ara available within the paper and its supplementary information files. Source data for all main fgures and supplementary are provided with the paper as indicated.

Research involving human participants, their data, or biological material

Policy information about studies with human participants or human data. See also policy information about sex, gender (identity/presentation), and sexual orientation and race, ethnicity and racism.

Reporting on sex and gender	N/A
Reporting on race, ethnicity, or other socially relevant groupings	N/A
Population characteristics	N/A
Recruitment	N/A
Ethics oversight	N/A

Note that full information on the approval of the study protocol must also be provided in the manuscript.

Field-specific reporting

Please select the one below that is the best fit for your research. If you are not sure, read the appropriate sections before making your selection.

☒ Life sciences ☐ Behavioural & social sciences ☐ Ecological, evolutionary & environmental sciences

For a reference copy of the document with all sections, see nature.com/documents/nr-reporting-summary-flat.pdf

Life sciences study design

All studies must disclose on these points even when the disclosure is negative.

Sample size	No statistical method was used to predetermine the sample sizes. For electrophysiology experiments, data sets are in line with the standards established in the field. the authors have extensive experience with data of this type and knowledge of tge typical data variability (e.g., Dawe et al. 2019, Neuron, Nakagawa, et al. 2024, Nature Structure and Molecular Biology).
Data exclusions	In electrophysiology experiments common control criteria in the field were applied (e.g. leak current, solution exchange rate). AMPAR complex assembly was evaluated based on receptor kinetics and linear I-V relationships as performed in Dawe, et al. 2019.
Replication	Data replicates of each experiments are detailed in the Methods and Results/figure legends. For electrophysiology experiments, each transfection condition was performed at least two independent times and the data pooled; all results were successfully replicated.
Randomization	Randomization is not relevant to electrophysiology experiments, as there are no experimental groups (data are oganized based on knoen receptor composition).
Blinding	No blinding was used in this study as it was not technically or practically feasible to do it.

Reporting for specific materials, systems and methods

We require information from authors about some types of materials, experimental systems and methods used in many studies. Here, indicate whether each material, system or method listed is relevant to your study. If you are not sure if a list item applies to your research, read the appropriate section before selecting a response.

Materials & experimental systems

n/a	Involved in the study
☒	☐ Antibodies
☐	☒ Eukaryotic cell lines
☒	☐ Palaeontology and archaeology
☐	☒ Animals and other organisms
☒	☐ Clinical data
☒	☐ Dual use research of concern
☒	☐ Plants

Methods

n/a	Involved in the study
☒	☐ ChIP-seq
☒	☐ Flow cytometry
☒	☐ MRI-based neuroimaging

Eukaryotic cell lines

Policy information about cell lines and Sex and Gender in Research

Cell line source(s)	HEK293T/17 (ATTC)
Authentication	No further authentication was performed for commercially available cell lines.
Mycoplasma contamination	Not tested specifically for this study
Commonly misidentified lines (See ICLAC register)	HEK cells are listed in the register; however, our cell lines comes from a reliable source and is the only cell line used in this study/by our lab, which minimizes the risk of any cross/contamination.

Animals and other research organisms

Policy information about studies involving animals; ARRIVE guidelines recommended for reporting animal research, and Sex and Gender in Research

Laboratory animals	Wild-type mice with a C57BL/6J background
Wild animals	The study did not involve wild animals
Reporting on sex	Sex was not considered (both sexes used).
Field-collected samples	The study did not involve samples collected from the field.
Ethics oversight	All experiments were performed in accordance with the guidelines of the Canadian Council on Animal Care and were approved by the Animal Care Committee of McGill University (approval #2013-7435).

Note that full information on the approval of the study protocol must also be provided in the manuscript.

Plants

Seed stocks	*Report on the source of all seed stocks or other plant material used. If applicable, state the seed stock centre and catalogue number. If plant specimens were collected from the field, describe the collection location, date and sampling procedures.*
Novel plant genotypes	*Describe the methods by which all novel plant genotypes were produced. This includes those generated by transgenic approaches, gene editing, chemical/radiation-based mutagenesis and hybridization. For transgenic lines, describe the transformation method, the number of independent lines analyzed and the generation upon which experiments were performed. For gene-edited lines, describe the editor used, the endogenous sequence targeted for editing, the targeting guide RNA sequence (if applicable) and how the editor was applied.*
Authentication	*Describe any authentication procedures for each seed stock used or novel genotype generated. Describe any experiments used to assess the effect of a mutation and, where applicable, how potential secondary effects (e.g. second site T-DNA insertions, mosiacism, off-target gene editing) were examined.*